Inverse modelling of European CH_4 emissions during 2006-2012 using different inverse models and reassessed atmospheric observations

Peter Bergamaschi[1], Ute Karstens[2,3], Alistair J. Manning[4], Marielle Saunois[5], Aki Tsuruta[6], Antoine Berchet[5,7], Alexander T. Vermeulen[3,8], Tim Arnold[4,9,10], Greet Janssens-Maenhout[1], Samuel Hammer[11], Ingeborg Levin[11], Martina Schmidt[11], Michel Ramonet[5], Morgan Lopez[5], Jost Lavric[2], Tuula Aalto[6], Huilin Chen[12,13], Dietrich G. Feist[2], Christoph Gerbig[2], László Haszpra[14,15], Ove Hermansen[16], Giovanni Manca[1], John Moncrieff[10], Frank Meinhardt[17], Jaroslaw Necki[18], Michal Galkowski[18], Simon O'Doherty[19], Nina Paramonova[20], Hubertus A. Scheeren[12], Martin Steinbacher[7], and Ed Dlugokencky[21]

[1] European Commission Joint Research Centre, Ispra (Va), Italy
[2] Max Planck Institute for Biogeochemistry, Jena, Germany
[3] ICOS Carbon Portal, ICOS ERIC, University of Lund, Sweden
[4] Met Office Exeter, Devon, UK
[5] Laboratoire des Sciences du Climat et de l'Environnement (LSCE-IPSL), CEA-CNRS-UVSQ, Université Paris-Saclay, F-91191 Gif-sur-Yvette, France
[6] Finnish Meteorological Institute (FMI), Helsinki, Finland
[7] Swiss Federal Laboratories for Materials Science and Technology (Empa), Dübendorf, Switzerland
[8] Energy research Centre of the Netherlands (ECN), Petten, Netherlands
[9] National Physical Laboratory, Teddington, Middlesex, TW11 0LW, UK
[10] School of GeoSciences, The University of Edinburgh, Edinburgh, EH9 3FF, UK
[11] Institut für Umweltphysik, Heidelberg University, Germany
[12] Center for Isotope Research (CIO), University of Groningen, Netherlands
[13] Cooperative Institute for Research in Environmental Sciences (CIRES), University of Colorado, Boulder, CO, USA
[14] Hungarian Meteorological Service, Budapest, Hungary
[15] Research Centre for Astronomy and Earth Sciences, Geodetic and Geophysical Institute, Sopron, Hungary
[16] Norwegian Institute for Air Research (NILU), Norway
[17] Umweltbundesamt, Messstelle Schauinsland, Kirchzarten, Germany
[18] AGH University of Science and Technology, Krakow, Poland
[19] Atmospheric Chemistry Research Group, University of Bristol, Bristol, UK
[20] Voeikov Main Geophysical Observatory, St. Petersburg, Russia
[21] NOAA Earth System Research Laboratory, Global Monitoring Division, Boulder, CO, USA

Correspondence to: Peter Bergamaschi (peter.bergamaschi@ec.europa.eu)

Supplementary Material

1. Atmospheric models

The atmospheric models used in this study are described in the following (see also Table 3 of paper).

1.1 TM5-4DVAR

The TM5-4DVAR inverse modelling system is described in detail by *Meirink et al.* [2008], and subsequent updates by *Bergamaschi et al.* [2010; 2015]. TM5-4DVAR is based on the two-way nested atmospheric zoom model TM5 [*Krol et al.*, 2005]. In this study we apply the zooming with 1°×1° resolution over Europe, while the global domain is simulated at a horizontal resolution of 6° (longitude) × 4° (latitude). TM5 is an offline transport model, driven by meteorological fields from the European Centre for Medium-Range Weather Forecasts (ECMWF) ERA-Interim reanalysis [*Dee et al.*, 2011]. Here, we employ an updated TM5 version using 3-hourly ERA-Interim interpolated meteorological fields (while previous versions used 6-hourly data for the 3-dimensional meteorological fields). 25 vertical layers are used (defined as a subset of the 60 layers of the ERA-Interim reanalysis). For non-resolved vertical mixing by deep and shallow cumulus convection the parameterisation of *Tiedtke* [1987] is used. Vertical turbulent mixing near the surface has been parameterised according to *Holtslag and Moeng* [1991], and in the free troposphere the parametric model of *Louis* [1979] is applied. The capability of TM5 to simulate the boundary layer dynamics has been evaluated in detail by *Koffi et al.* [2016].

The 4-dimensional variational (4DVAR) optimization technique minimizes iteratively a cost function using the adjoint of the tangent linear model [*Krol et al.*, 2008; *Meirink et al.*, 2008] and the m1qn3 algorithm [*Gilbert and Lemaréchal*, 1989] for minimization. We apply a 'semi-lognormal' description of the probability density function for the 'a priori' emissions to force the 'a posteriori' emissions to remain positive [*Bergamaschi et al.*, 2010; *Bergamaschi et al.*, 2015]. In inversions S1, S2, and S4, four groups of CH_4 emissions are optimized independently: (1) wetlands, (2) rice, (3) biomass burning, and (4) all remaining sources [*Bergamaschi et al.*, 2015]. We assume uncertainties of 100% per grid-cell and month for each source group and apply a spatial correlation scale length of 200 km in S1, S2, and S4. The temporal correlation timescales are set to zero for wetlands, rice, and biomass burning, and 12 months for the 'remaining' CH_4 sources. In S3, only total emissions are optimized, using a homogeneous distribution of emissions over land and over the ocean, respectively, as starting point for the optimization (as described in *Bergamaschi et al.* [2010; 2015]). In this case, uncertainties of 500% per grid-cell and month, a spatial correlation scale length of 50 km, and a temporal correlation timescale of 1 month are applied. The photochemical sinks of CH_4 in the troposphere (OH), and stratosphere (OH, Cl, and $O(^1D)$) are simulated as described in *Bergamaschi et al.* [2010]. For the continuous CH_4 measurements from the InGOS stations, the given "working standard repeatability" (see section 2 of main paper) has been used as observation error (using a minimum error of 3 ppb), while for the discrete air samples a constant observation error of 3 ppb was applied. The model representation error is estimated as a function of local emissions and 3-dimensional gradients of simulated mole fractions [*Bergamaschi et al.*, 2010].

1.2 TM5-CTE

The TM5-CTE inverse modelling system is described in detail by *Tsuruta et al.* [2016]. The system uses TM5 similarly to TM5-4DVAR, but with a slightly different zoom area that extends to northern Europe (up to 74°N latitude). As TM5-4DVAR, it uses 25 vertical layers and pre-calculated 3-hourly meteorology from ECMWF ERA-Interim reanalysis. The photochemical sink of CH_4 due to tropospheric and stratospheric OH, and stratospheric Cl and $O(^1D)$ was pre-calculated based on *Houweling et al.* [2014] and *Brühl and Crutzen* [1993] and not adjusted in the optimization scheme. The optimization scheme is based on the ensemble Kalman filter [*Evensen*, 2003], with a fixed-lag smoother [*Ravela and McLaughlin*, 2007]. Emissions were optimized region-wise at weekly (7 days) resolution with an ensemble size of 500 and a lag of 5 weeks. In this study, we report monthly emission estimates aggregated from the weekly estimates. Regions were defined based on 15 modified TransCom regions and six land-ecosystem types (LET) [*Tsuruta et al.*, 2016]. Overall, the number of regions optimized was 58 globally. In inversion S1, S2 and S4, CH_4 emission estimates for anthropogenic and biospheric (LPX-Bern v1.0 [*Spahni et al.*, 2013]) sources were optimized independently. In addition, CH_4 emission estimates for biomass burning (GFED v3 [*Randerson et al.*, 2013; *van der Werf et al.*, 2010], termites [*Ito and Inatomi*, 2012], and ocean [*Lambert and Schmidt*, 1993] were included, but these were not optimized in the system. In the flat prior inversion (S3), the sum of anthropogenic and biosphere emission sources were optimized.

In all inversions, the prior uncertainty was assumed 80% of the emissions per region. Errors in the prior emissions were assumed to be uncorrelated between the different LETs. Within each LET, the spatial correlation scale length was set to 900 km. Observation errors were assumed to be uncorrelated in space and time. The observation errors were defined based on the transport model and measurement errors, resulting in overall errors in the range 7.5 ppb to 914 ppb.

1.3 LMDZ-4DVAR

The LMDz-PYVAR inverse system is based on the offline and adjoint models of the Laboratoire de Météorologie Dynamique, version 4 (LMDz) general circulation model [*Hourdin and Armengaud*, 1999; *Hourdin et al.*, 2006]. LMDz-PYVAR uses pre-computed air masses by the LMDz on-line general circulation model nudged to the ERA-Interim horizontal wind to get appropriate meteorology. The LMDz-PYVAR inverse system has been extensively described in *Chevallier et al.* [2005] and in *Pison et al.* [2009] for LMDz-PYVAR-SACS, which includes the oxidation chain of methane. Here the zooming capability of the model has been applied over Europe as in *Bergamaschi et al.* [2015]. Using the zoom, the model grid is stretched in order to get a resolution of around 1.2°(longitude) × 0.8°(latitude) resolution over Europe while keeping the same number of horizontal grid cells (96 in longitude and 73 in latitude), leading to a maximum grid size of 7.2°×3.6°. In the vertical, 19 hybrid pressure levels extend from the surface to about 3 hPa. This corresponds to a vertical resolution of about 300-500 m in the planetary boundary layer (first level at 70 m height) and to a resolution of about 2 km at the tropopause (with 7-9 levels in the stratosphere). The 4-dimensional variational optimization technique minimizes iteratively a cost function using the adjoint of the tangent linear model and the M1QN3 algorithm for minimization [*Gilbert and Lemaréchal*, 1989]. The chemistry module includes sinks of methane through tropospheric and stratospheric OH and stratospheric $O(^1D)$ oxidation. The total net emissions of methane are optimized at the grid-cell resolution for 8-days periods. Uncertainties are set at 100% per grid-cell and per period with a spatial correlation scale length of 500 km for all inversions, except inversion S3 where the uncertainties were set at 200%. The given "working standard repeatability" provided for the INGOS sites has been used as observation error (using a minimum error of 3 ppb). For other sites a constant observations error of 3 ppb was applied. The model error, larger than the instrumental error, has been quadratically added and depends on the model performance at each site, ranging from 15 ppb to 100 ppb. The OH concentration fields are based on the Transcom OH dataset [*Patra et al.*, 2011; *Spivakovsky et al.*, 2000] and are simultaneously inverted using methyl-chloroform observations [*Pison et al.*, 2009].

1.4 TM3-STILT

In the Jena inversion system, regional-scale high-resolution inversions are performed with the coupled TM3-STILT system. TM3-STILT [*Trusilova et al.*, 2010] is based on a combination of the fine-scale regional Stochastic Time-Inverted Lagrangian Transport model STILT [*Gerbig et al.*, 2003; *Lin et al.*, 2003] and the coarse-grid global 3-dimensional atmospheric offline transport model TM3 [*Heimann and Koerner*, 2003], coupled according to the two-step nesting scheme of *Rödenbeck et al.* [2009]. This nesting scheme allows the use of completely independent models for the representation of global and regional transport and hence facilitates an easy exchange of either component. The same variational inversion algorithm [*Rödenbeck*, 2005] is applied in the global and in the regional inversion step of the Jena inversion system. In this study, the global transport model TM3 is used with a spatial resolution of 4°×5° and 26 vertical levels, driven by 3-hourly ERA-Interim reanalysis [*Dee et al.*, 2011]. STILT is driven by meteorological fields from ECMWF operational analysis, used here with a spatial resolution of 0.25°×0.25° and confined to the lowest 61 vertical layers. The regional TM3-STILT inversions are conducted in this study on a 0.25°×0.25° horizontal resolution grid covering the greater part of Europe (15°W-35°E, 33°N-73°N). Chemical processes are only taken into account in the global model simulations, where the photochemical sinks of CH_4 are parameterized using the same pre-optimized monthly OH fields and stratospheric sink as described in *Patra et al.* [2011]. On the regional scale CH_4 is treated as a conservative tracer because of its relatively long lifetime. In all TM3-STILT inversions, the total emissions are optimized. Uncertainties of 100% per grid cell and month, with a spatial correlation scale length of 300 km and a temporal correlation time scale of 1 month, are assumed in the regional inversions S1, S2, and S4, whereas the uncertainties are set to 500% with a correlation scale length of 60 km in S3. The repeatability reported for the InGOS data set was used as estimate of the observation error. For all other stations the observation error was set to 3 ppb. Model representation errors are assigned to the individual sites according to their location with respect to continental, remote or oceanic situations [*Rödenbeck*, 2005], ranging from 45 ppb to 15 ppb, respectively.

Sensitivity studies for S1 are also carried out using the same modular nesting technique to couple STILT with the global baseline provided by TM5-4DVAR results for the S4 case. The regional inversion step itself is again performed in the Jena inversion system. This combination is referred to as TM5-STILT in the presentation of results.

1.5 NAME

The Met Office's inverse modelling system (InTEM = Inversion Technique for Emission Modelling) using the NAME Lagrangian atmospheric dispersion model has evolved since the work of *Manning et al.* [2011] and the NitroEurope project [*Bergamaschi et al.*, 2015] and is now based on a Bayesian methodology. Measurement uncertainty reported in the InGOS data set was used as observation error. Model-measurement mismatch errors were also applied to each measurement and they were calculated using a metric based on the modelled wind speed and boundary layer height. Times of low wind speed or boundary layer height were assigned high uncertainty on a sliding scale depending on these values. In addition these model errors were inflated based on the difference between the model release height above sea level and the true altitude of the observation. 200 km horizontal and 12 hour observation correlations were applied in the inversions. Grid boxes (0.5625° × 0.375° for period 01/2006-03/2010 and 0.3516° × 0.2344° for 03/2010-12/2012) were aggregated based on the sensitivity of measurements to emissions, creating around 100-150 course grid regions within the inversion domain (23.8° W - 39.2° E, 31.6° N - 79.6° N). A non-negative least square solver was used to optimise the solution thus preventing negative emissions from being estimated. The prior grid of emissions was given an uncertainty so that the UK had an aggregated uncertainty of 40%. All measurements were included in the inversion, averaged into 3-hourly time periods, except those from the high altitude mountain stations Jungfraujoch (JFJ), Pic du Midi (PDM), and Kasprowy Wierch (KAS). These were considered to have a too severe mismatch between the modelled and actual altitude to be correctly interpreted. A total of eleven extra 'boundary condition' variables were estimated as part of the inversion. The CH_4 composition of air arriving into the domain was considered a variable within the inversion. A prior time-series was calculated using data at Mace Head when well-mixed 'clean' air arrived from the North Atlantic Ocean and the inversion then used eleven multiplying factors to calculate posterior mole fractions of the background air arriving from eight horizontal (SSE, SSW, WSW,…, ESE) boundaries at 0-6 km, two boundaries (north and south) from 6 to 9 km, and a boundary at 9 km (upper troposphere to stratosphere).

1.6 CHIMERE

The CHIMERE inversion system is fully described and evaluated in *Berchet et al.* [2015a; 2015b]. It relies on forward transport simulations with the Eulerian mesoscale chemistry transport model CHIMERE [*Menut et al.*, 2013] on a limited-area domain covering all Europe. The transport operator **H** is explicitly computed from the influence of a set of separated "emission regions" (50 emission sub-regions in Europe + boundary conditions interpolated at the border of the CHIMERE domain from LMDz global simulations as described in *Bousquet et al.* [2011]) on the observation sites. The 3-dimensional domain embraces roughly all the troposphere with 29 vertical layers geometrically spaced from the surface to 300 hPa. The domain is simulated with a horizontal resolution of 40 km x 40 km, with meteorological fields interpolated from 3-hourly ECMWF ERA-Interim reanalysis. The CHIMERE inversion system is an analytical system explicitly solving the posterior state vector $\mathbf{x}^a$ and posterior uncertainties $\mathbf{P}^a$. To account for the uncertainties in the prior error matrices **R** and **B**, the posterior probability density function $p(\mathbf{x} \mid \mathbf{y}^0 - \mathbf{H}\mathbf{x}^b, \mathbf{x}^b)$ is computed as a weighted sum of the marginal Gaussian pdfs $p(\mathbf{x} \mid \mathbf{y}^0 - \mathbf{H}\mathbf{x}^b, \mathbf{x}^b, \mathbf{R}, \mathbf{B})$. This so-called marginalized inversion is implemented through a Monte-Carlo experiment of 60’000 (**R**, **B**) matrix couples. The distribution of possible (**R**, **B**) couples in the Monte Carlo sampling is deduced from a maximum likelihood algorithm following *Dee* [1995]. Therefore, uncertainty matrices are computed in the inversion system itself, and not prescribed based on expert knowledge. The system is applied to scenario S4 for the year 2010 only.

1.7 COMET

The COMET model is a Lagrangian model that can be used for both predictive and inverse modelling purposes [*Eisma et al.*, 1995; *Vermeulen et al.*, 1999; *Vermeulen et al.*, 2006]. COMET uses backward trajectories to establish the source-receptor relationship, the so-called source-receptor matrix (SRM). The calculations described in this paper were performed using trajectory and mixing layer height data derived from 3-hourly resolution ECMWF ERA-Interim meteorological data at 1 degree longitude / latitude resolution, interpolated to 10 × 10 minutes (0.17° × 0.17°) resolution. All 60 vertical model layers of the ERA-Interim are used in the FLEXTRA V5 trajectory model [*Stohl and Seibert*, 1998] to calculate 3-D 144 h backward trajectories from the ECMWF wind fields for all observation stations and arrival heights. The GRIB encoded fields required by FLEXTRA were generated using the FLEXPART/FLEXTRA preprocessing routines V4.

To account for mixing of the source signal in the planetary boundary layer with the free troposphere, two vertical layers are distinguished in the COMET model, a mixing layer and a reservoir layer. The initial tracer concentration at the start of each trajectory is taken in this case from the TM5-4DVAR optimised concentration fields at 1°×1° resolution over Europe and at global 6°×4° resolution (outside the European TM5 zoom domain) depending on the location. The height of the planetary boundary layer is taken from the ECMWF analysed BLH (GRIB code 159 parameter). All emissions are first accumulated in this mixed layer and when the mixed layer height changes, mass transfer takes place with the reservoir layer.

The area that influences the concentrations in the column of air in the mixed layer is assumed to be circular and the diameter of this circle is assumed to change linearly with travel time; from large (80 km) at the start (-144 hours) of the backward trajectory to small (20 km) at the destination. This cone-shaped trajectory path defines a highly simplified parametrised form of the real region of influence, determined by advection, convection and turbulent diffusion.

In inverse mode the model stores for each time step the sensitivity to emissions on a grid of 0.1°×0.1° within the domain over western Europe and the difference between measured concentration **C** and background concentration $\mathbf{C_{back}}$ at the start of each trajectory. Tall tower measurements are evaluated using all measurements below the instantaneous BLH at the position of the tower as best estimate of the bulk concentration in the mixed layer. When the trajectory is at any point in time above the boundary layer, no sensitivity is added for that point. When the BLH changes the whole sensitivity matrix for that time step is scaled with the calculated dilution factor between reservoir and mixed layer.

The accumulated sensitivity matrix over an evaluation period is normalized by finding the grid square with maximum sensitivity. Starting from that point a recursive routine aggregates neighbouring grid points two by two until the joined area has a sensitivity equal or larger than the maximum. This reduces the sensitivity matrix **S** of 400×600 to a vector **s** of about 200 emission regions with members filled with numbers of the same order of magnitude, thereby improving stability of the following inversion routine. For each aggregated grid area also the average emission for each region is calculated as a prior emission estimate vector **E**. The system **C-C**$_{\mathbf{back}}$=**E.s** is solved for the unknown values of **E** using a Singular Value Decomposition method [*Press et al.*, 1992]. Areas with high variability of the best fitting emission are assigned the prior emission value for that region (contributions from these areas are removed from the **C-C**$_{\mathbf{back}}$ vector), and areas with high covariance with other areas are aggregated. The SVD inversion is repeated recursively until a stable solution has been reached. The COMET inversion method has been tested extensively and always reaches an excellent fit with aggregated prior emissions in synthetic inversions, despite the distortion of the source areas into lumped areas due to the aggregation. It could be applied to any SRM, including those from more sophisticated LPDM's, but is applied here to a simple trajectory model as this enables the system to do a full inversion for a one year period on a single PC in about 15 minutes.

2. Evaluation of integrated enhancement of observations and model simulations compared to the background

The enhancement of observations and model simulations are compared to the background mole fractions, (1) integrated over the entire boundary layer, and (2) integrated over the lower troposphere up to ~3-4 km. The background mole fractions are calculated by TM5 (based on the scheme of *Rödenbeck et al.* [2009]), using the TM5 zoom domain (which is the domain shown in Figure 2 and Figures 1S-3S) as common reference for observations and all models. For comparison, also the background mole fractions for the STILT and NAME domains are calculated.

The enhancement of measurements and model simulations compared to the background mole fractions, integrated over the boundary layer, are denoted as $\Delta c_{MOD\ BL}$ and $\Delta c_{OBS,\ BL}$, respectively, and are evaluated as follows:

$$\Delta c_{OBS,BL} = \frac{1}{p_{surf} - p_{BLH}}\left[(p_{surf} - p_1)\,(c_{OBS,1} - c_{BG,1}) + \sum_{i=1}^{k-1}(p_i - p_{i+1})\frac{(c_{OBS,i} - c_{BG,i}) + (c_{OBS,i+1} - c_{BG,i+1})}{2} + (p_k - p_{BLH})\,(c_{OBS,k} - c_{BG,k})\right]$$

and

$$\Delta c_{MOD,BL} = \frac{1}{p_{surf} - p_{BLH}}\left[(p_{surf} - p_1)\,(c_{MOD,1} - c_{BG,1}) + \sum_{i=1}^{k-1}(p_i - p_{i+1})\frac{(c_{MOD,i} - c_{BG,i}) + (c_{MOD\ i+1} - c_{BG,i+1})}{2} + (p_k - p_{BLH})\,(c_{MOD,k} - c_{BG,k})\right]$$

where p_{surf} is the surface pressure (taken from ECMWF ERA-INTERIM based meteorological fields in TM5), p_i the pressure at which aircraft measurements were taken, $c_{OBS,i}$, $c_{MOD,i}$, $c_{BG,i}$ the dry air mole fractions of observations, model simulations, and (simulated) background, respectively (for level i). p_k is the uppermost level within the boundary layer, and p_{BLH} the pressure of the top of the boundary layer (taken from TM5). The applied formula implies extrapolation of the lowermost measurement ($c_{OBS,i}$) (or model simulations) to the surface and of the uppermost measurements ($c_{OBS,k}$) (or model simulation) to the top of the boundary layer. We use only profiles for which (1) at least 2 measurements within the boundary layer are available, (2) $\Delta c_{OBS,\ BL}$ is equal or greater than 10 ppb, and (3) the boundary layer is at least 500 m.

The integration over the total column (lower troposphere) is performed in a similar way, using the entire profile (for ORL, HNG, and BIK), typically extending up to ~3-4 km (and without any extrapolation of the uppermost sample)

$$\Delta c_{OBS,COL} = \frac{1}{p_{surf} - p_k}\left[\left(p_{surf} - p_1\right)\left(c_{OBS,1} - c_{BG,1}\right) + \sum_{i=1}^{k-1}\left(p_i - p_{i+1}\right)\frac{\left(c_{OBS,i} - c_{BG,i}\right) + \left(c_{OBS,i+1} - c_{BG,i+1}\right)}{2}\right]$$

and

$$\Delta c_{MOD,COL} = \frac{1}{p_{surf} - p_k}\left[\left(p_{surf} - p_1\right)\left(c_{MOD,1} - c_{BG,1}\right) + \sum_{i=1}^{k-1}\left(p_i - p_{i+1}\right)\frac{\left(c_{MOD,i} - c_{BG,i}\right) + \left(c_{MOD,i+1} - c_{BG,i+1}\right)}{2}\right]$$

For the IMECC profile an explicit upper integration limit of 4 km is applied.

Only profiles for which $\Delta c_{OBS,\,COL}$ is equal or greater than 10 ppb are evaluated further.

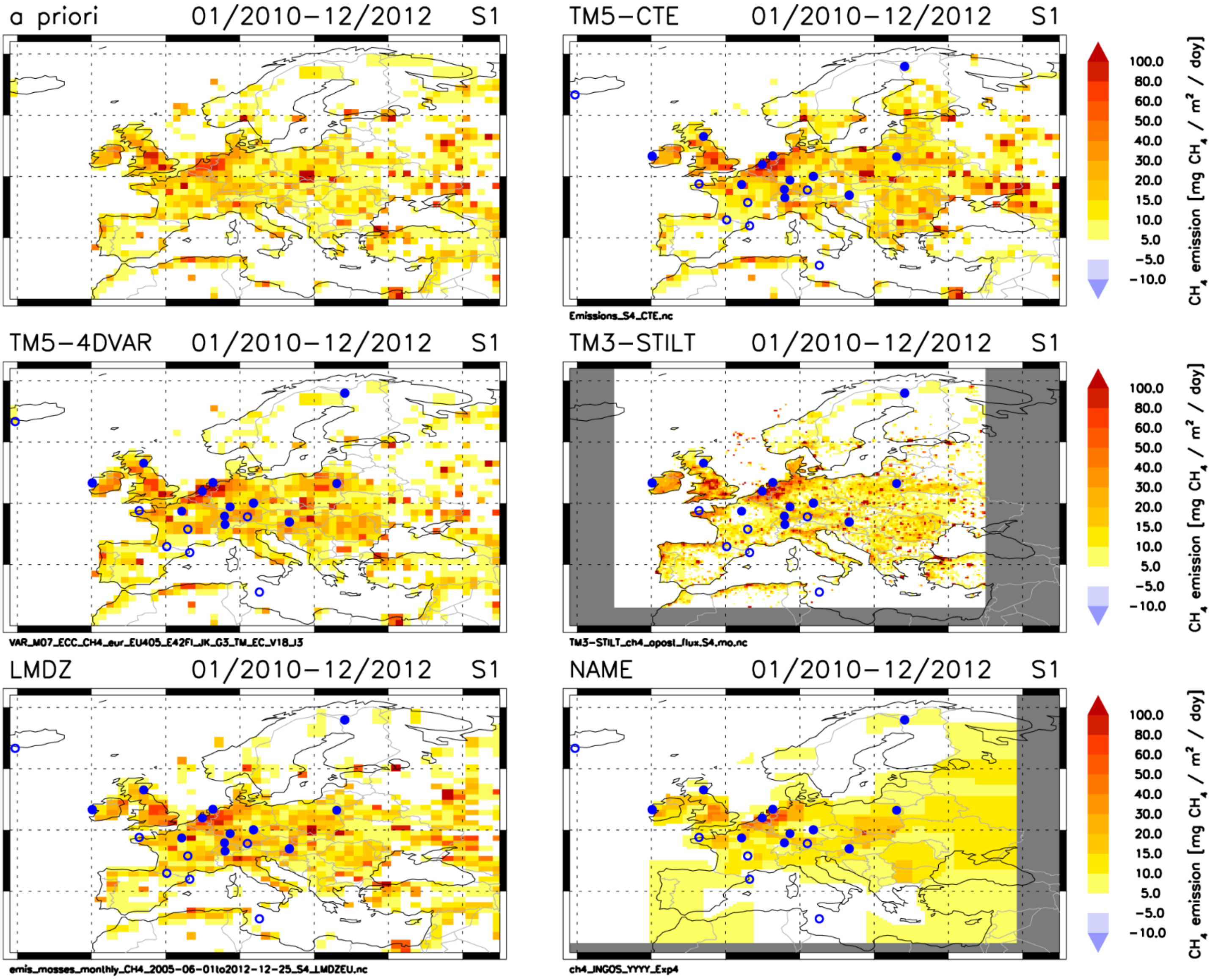

Figure 1S: European CH_4 emissions (average 2010–2012) for inversion S1. Filled blue circles are InGOS measurement stations with in-situ measurements, open circles are discrete air sampling sites. Upper left panel shows a priori CH_4 emissions (as applied in TM5-4DVAR at 1°×1° resolution).

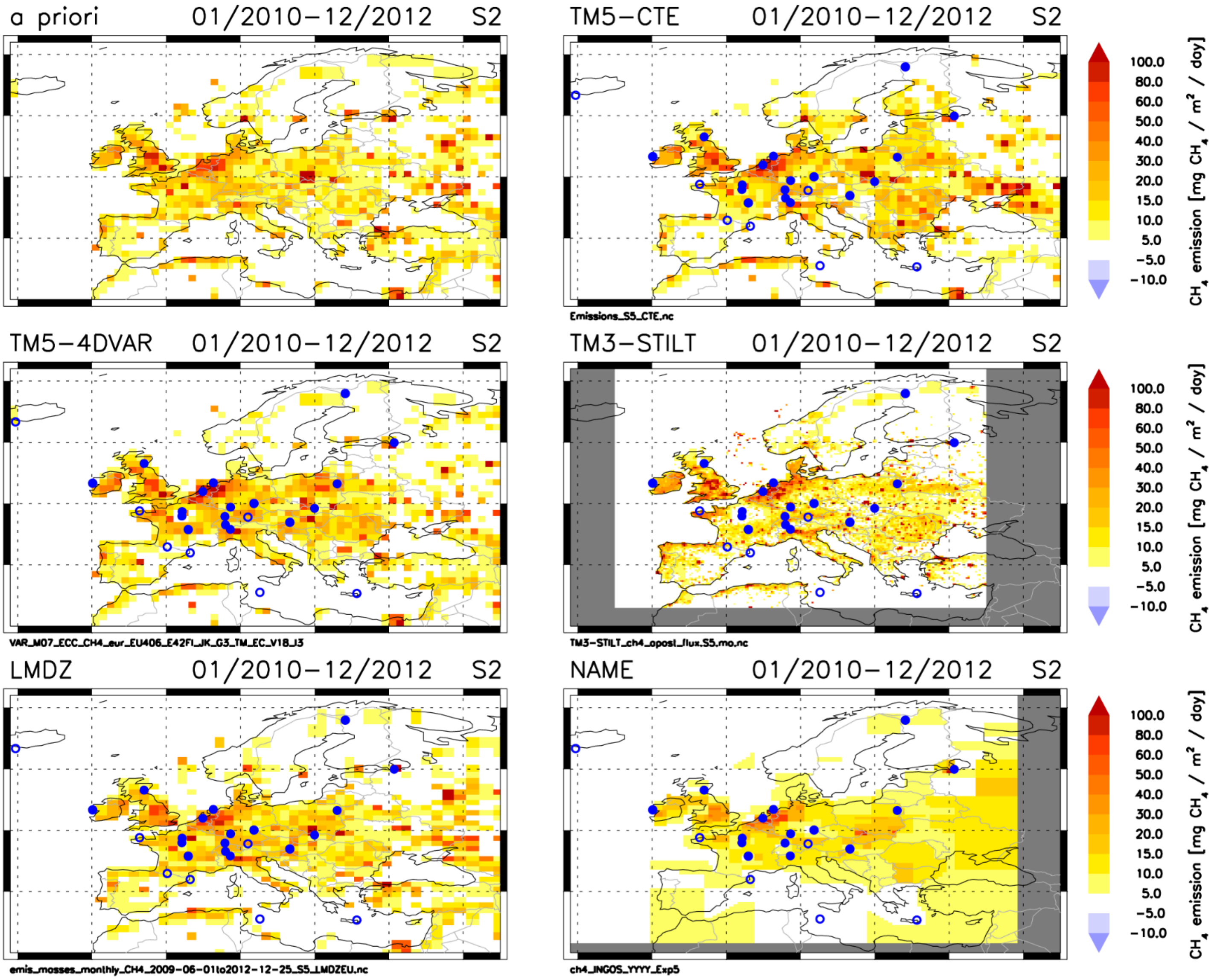

45 **Figure 2S:** European CH_4 emissions (average 2010–2012) for inversion S2. Filled blue circles are InGOS measurement stations with in-situ measurements, open circles are discrete air sampling sites. Upper left panel shows a priori CH_4 emissions (as applied in TM5-4DVAR at 1°×1° resolution).

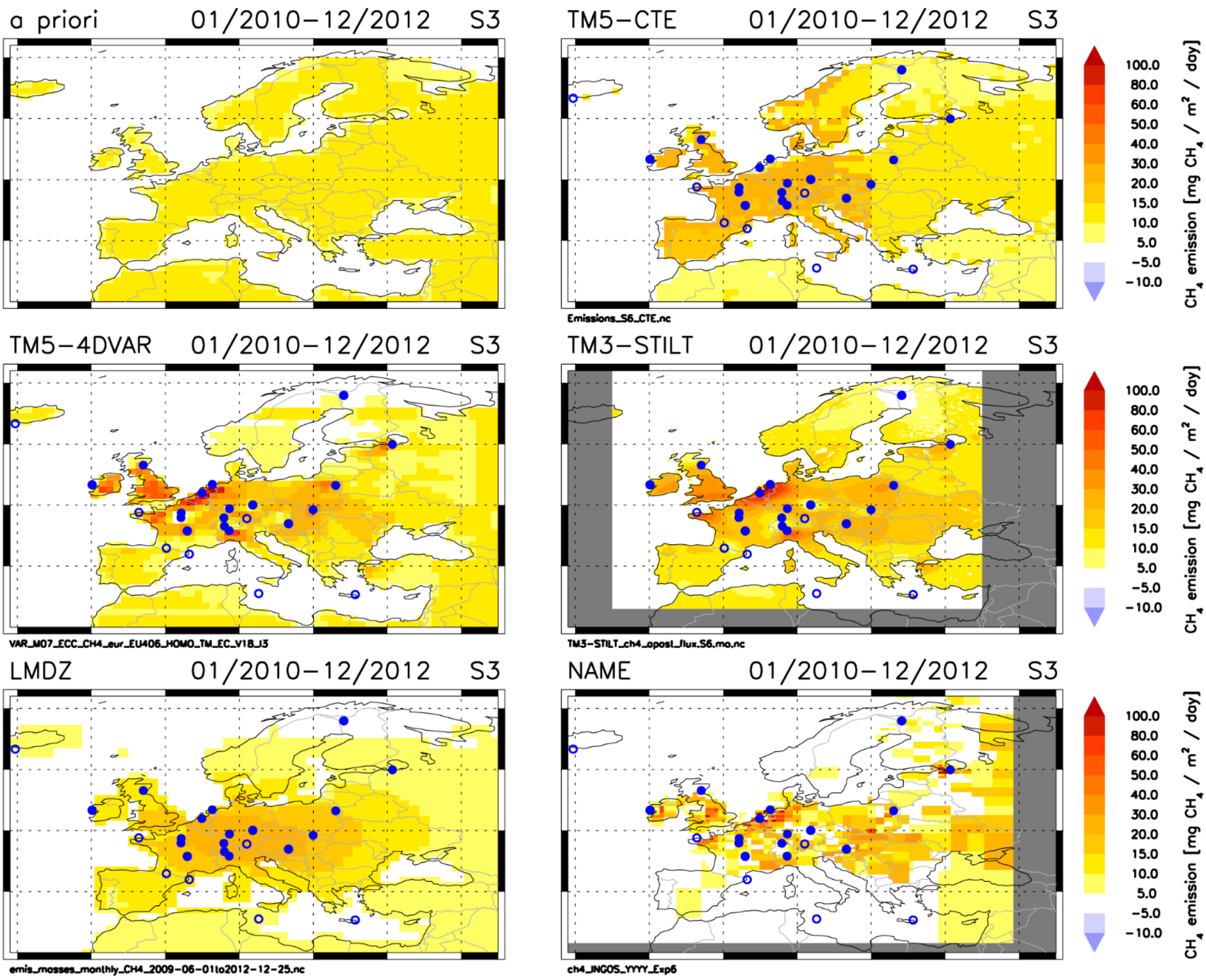

Figure 3S: European CH_4 emissions (average 2010–2012) for inversion S3. Filled blue circles are InGOS measurement stations with in-situ measurements, open circles are discrete air sampling sites. Upper left panel shows the homogeneous distribution of emissions over land (and over the ocean; not visible in chosen colour scale because of low magnitude), as applied in TM5-4DVAR as starting point for the optimization (as "weak a priori").

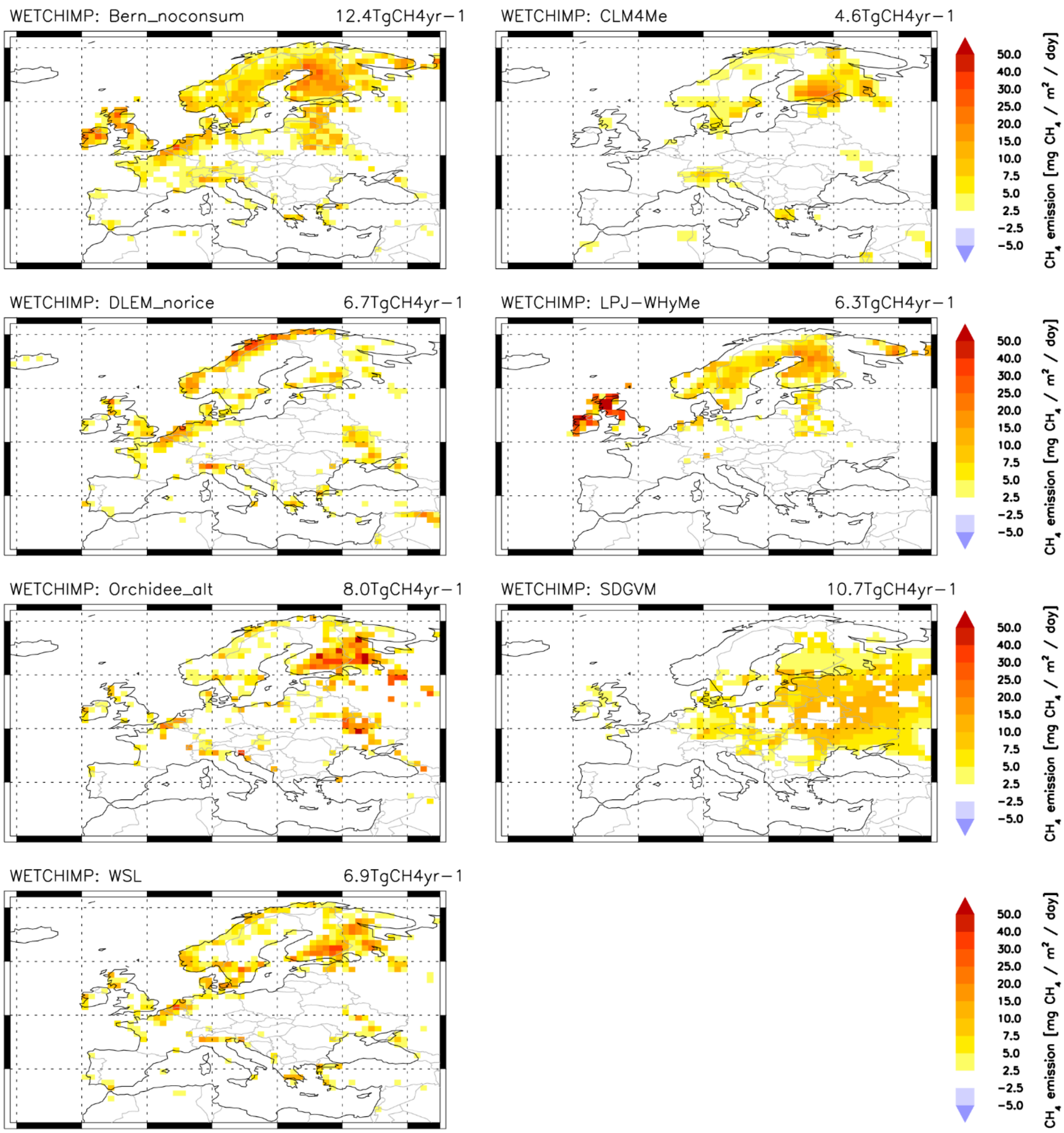

Figure 4S: European wetland CH_4 emissions (average 1993-2004) from different wetland models of the "Wetland and Wetland CH_4 Inter-comparison of Models Project" (WETCHIMP) [*Melton et al.*, 2013; *Wania et al.*, 2013].

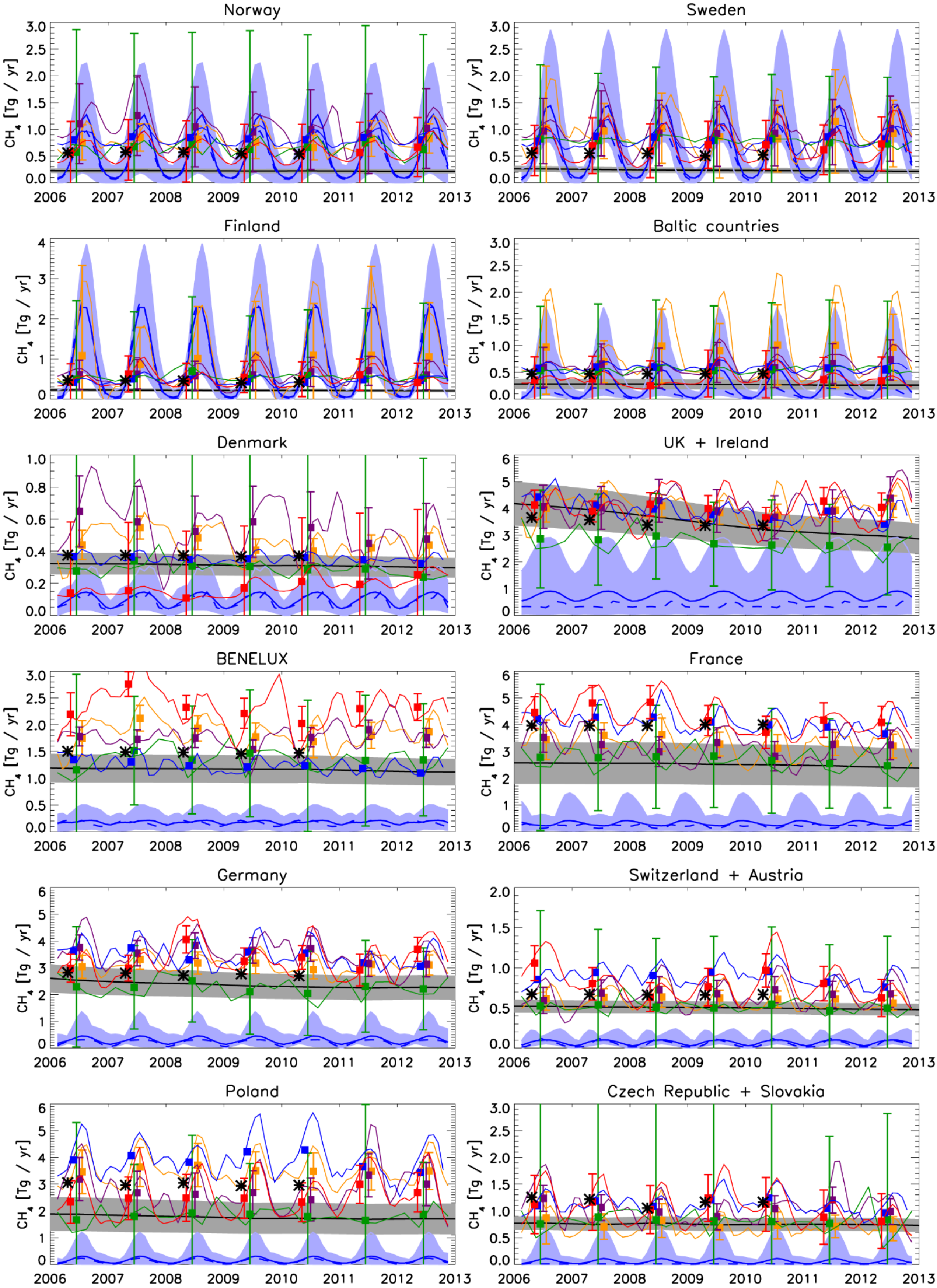

Figure 5S: Annual total (coloured symbols) and seasonal variation (coloured solid lines) of CH_4 emissions derived from inversions for European countries. For comparison, anthropogenic CH_4 emissions reported to UNFCCC (black line), and from EDGARv4.2FI.(black stars) are shown. Furthermore, the blue lines show wetland CH_4 emissions from the WETCHIMP ensemble of seven models (mean (blue solid line); median (blue dashed line); minimum-maximum range (light-blue range)).

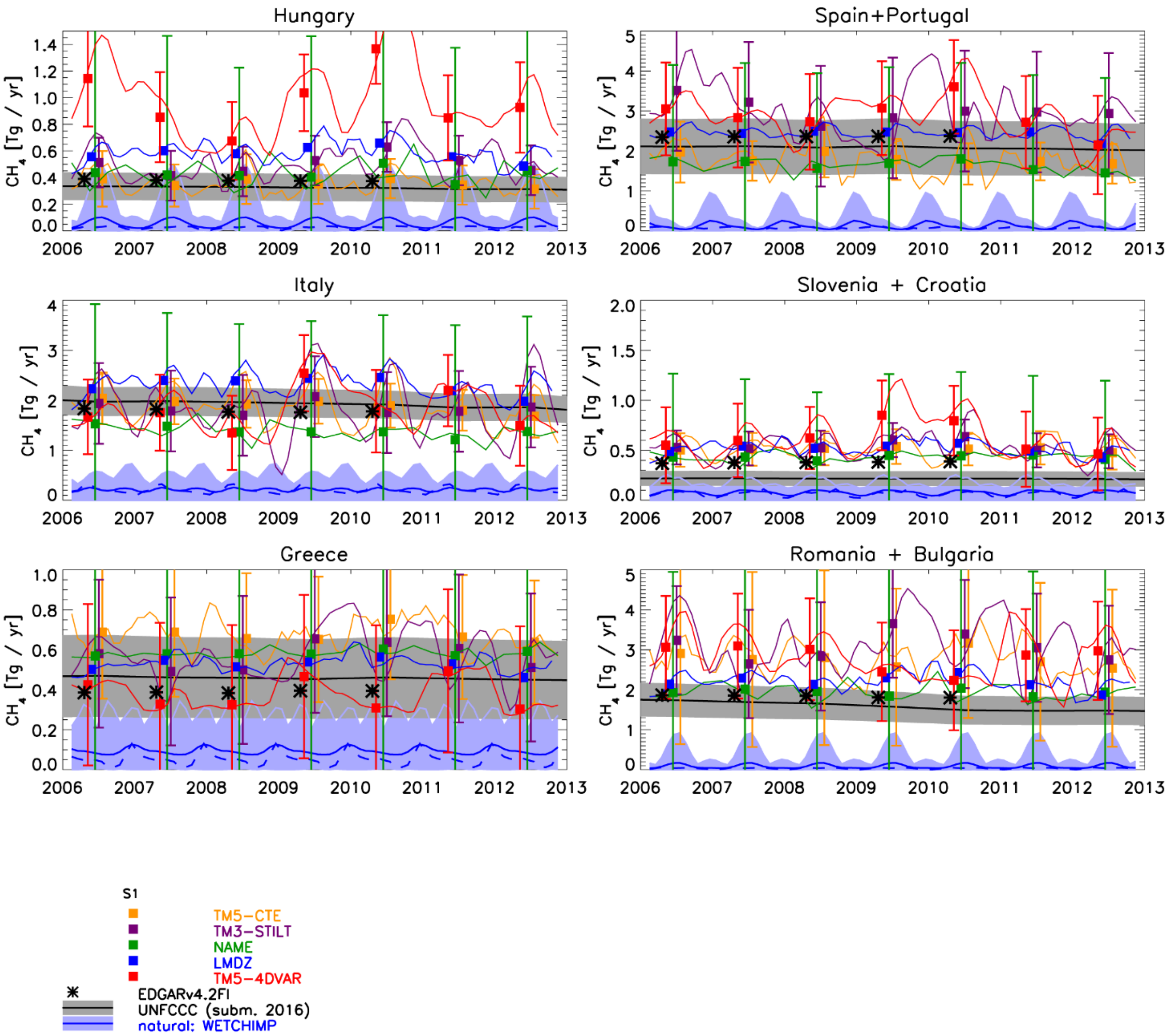

Figure 5S (continued)

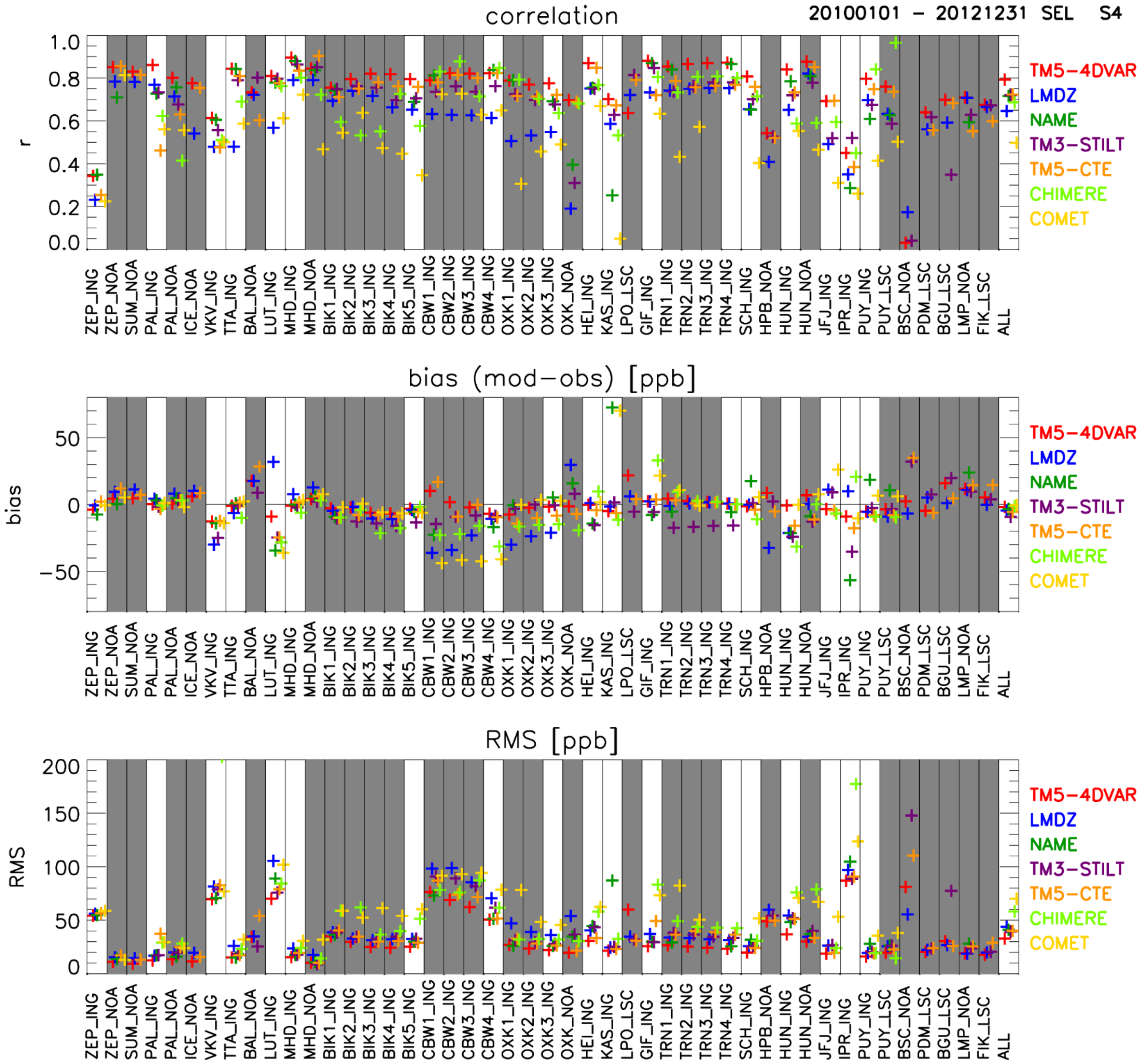

Figure 6S: Comparison of modelled and observed CH_4 at European monitoring stations: correlation coefficients r (top), bias (middle), and root mean square (RMS) differences (bottom) for inversion S4. 'All' denotes the mean correlation coefficient, bias and RMS difference, averaged over those stations, for which results were available from all models. White background indicates stations that were assimilated in inversion S4, and grey background stations that were used for validation only.

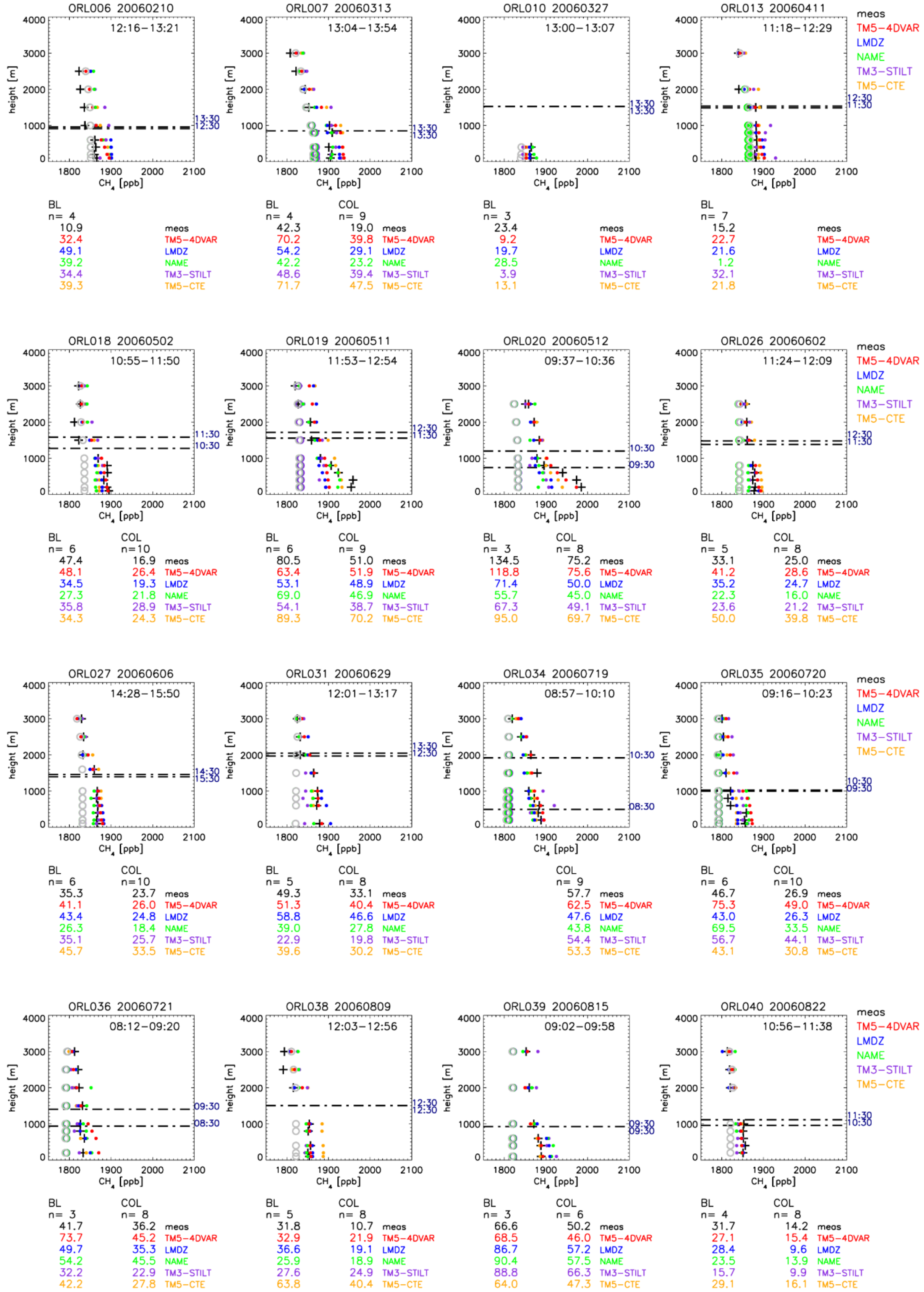

Figure 7S: Individual aircraft profiles from Orléans (ORL), France. Black crosses: measurements; filled coloured symbols: corresponding model simulations; open circles: simulated background mole fractions, based on the method of *Rödenbeck et al.* [2009], calculated for the TM5 domain (grey), and for the NAME (green) and TM3-STILT (violet) domains (the latter are, however, only partially visible, since they largely overlap with the background for the TM5 domain). Below each panel the calculated enhancements integrated over the entire boundary layer ($\Delta c_{MOD,\,BL}$ and $\Delta c_{OBS,\,BL}$) and integrated over the entire profile ($\Delta c_{MOD,\,COL}$ and $\Delta c_{OBS,\,COL}$) are given. n denote the number of samples used to evaluate the integrated enhancements. The dash-dotted lines indicate the top of the boundary layer diagnosed by TM5 at the given times.

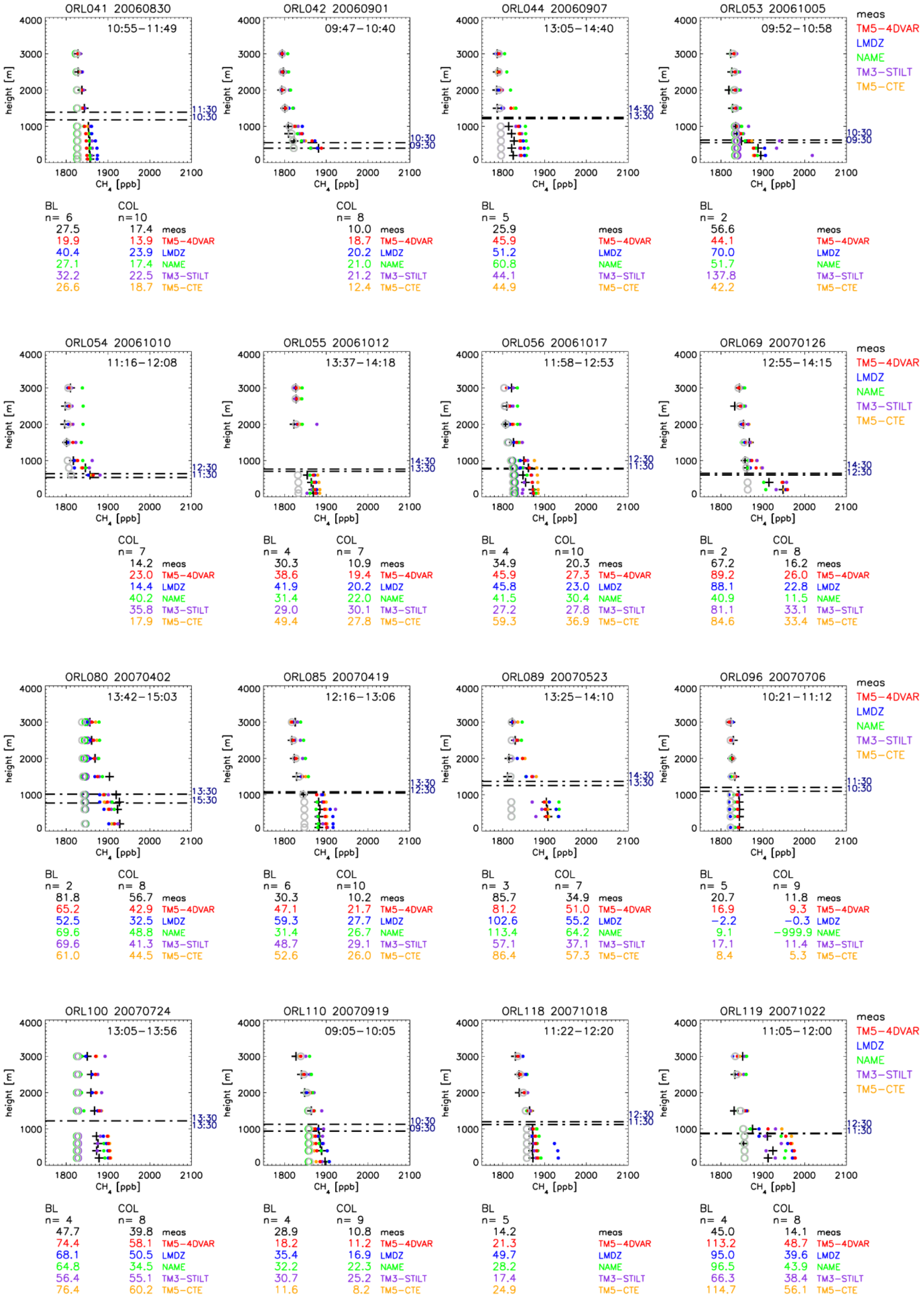

Figure 7S: continued

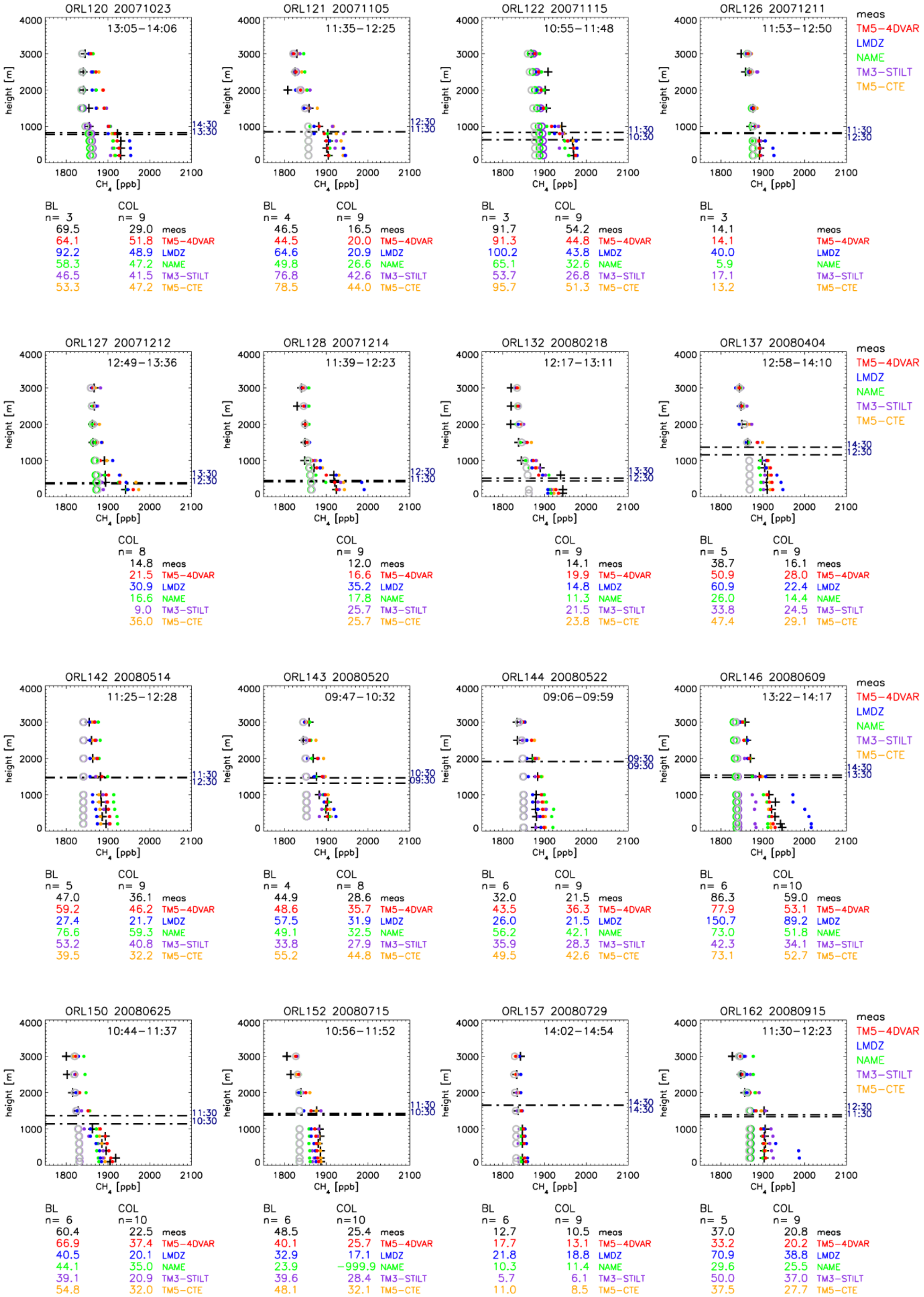

Figure 7S: continued

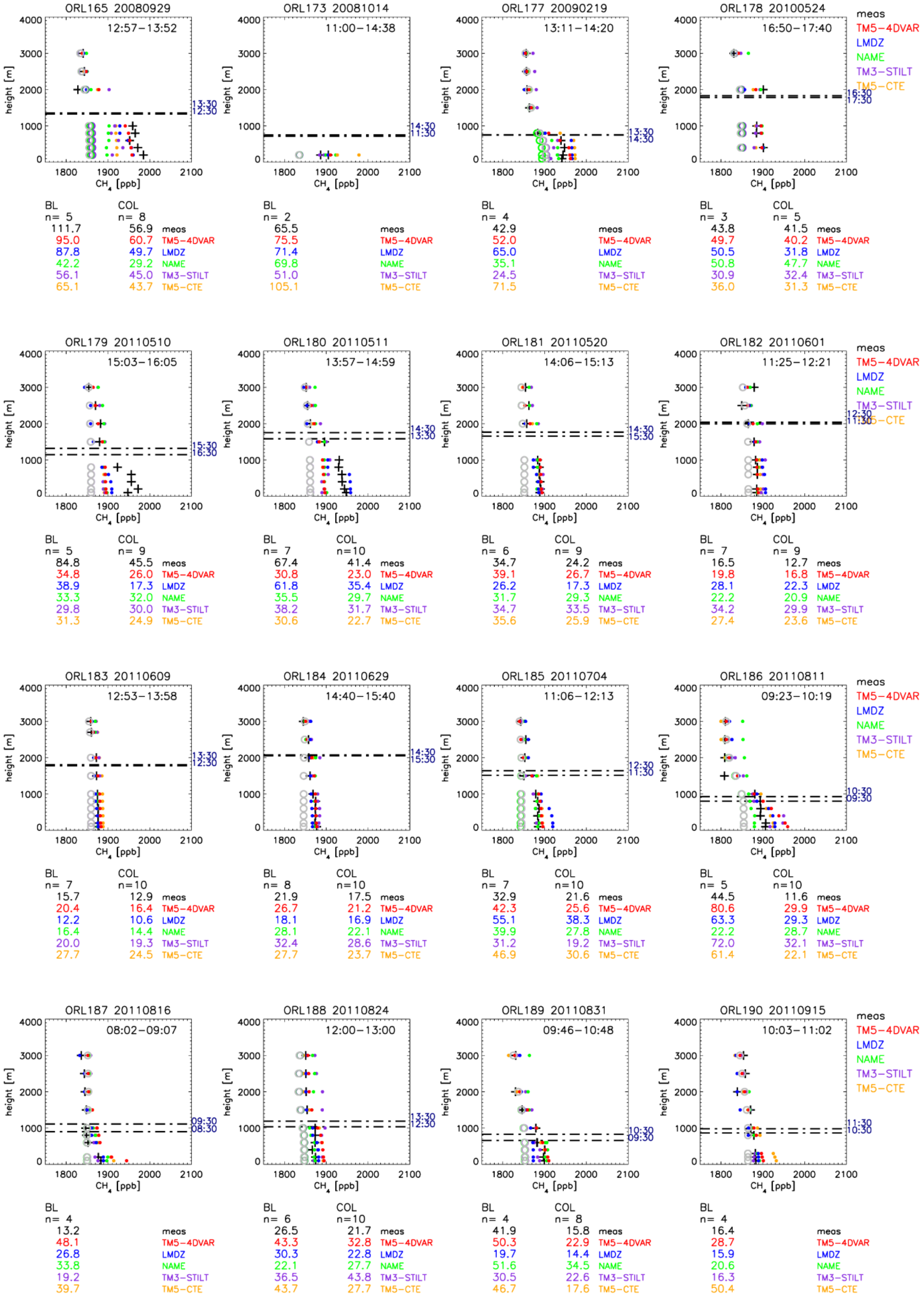

Figure 7S: continued

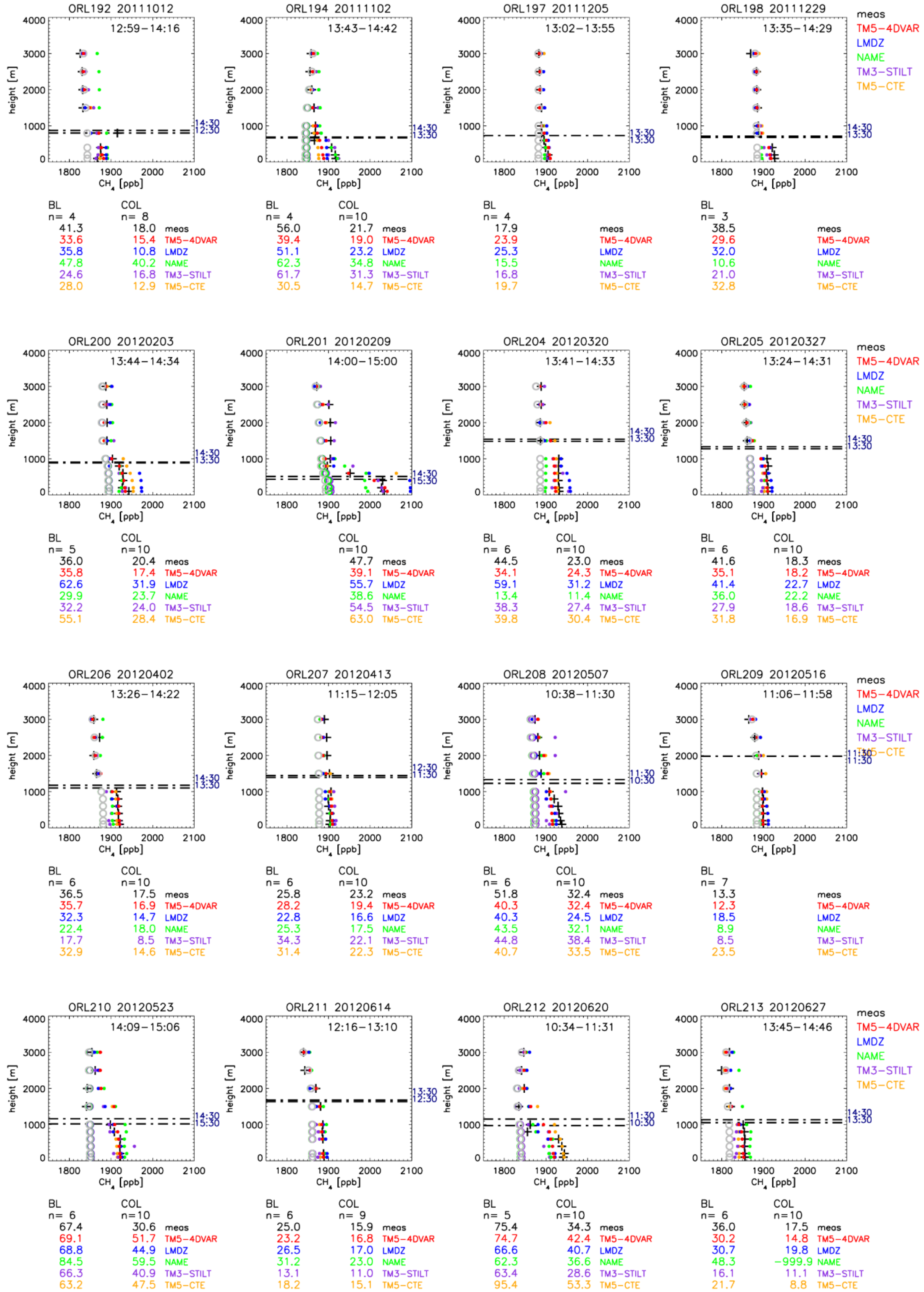

Figure 7S: continued

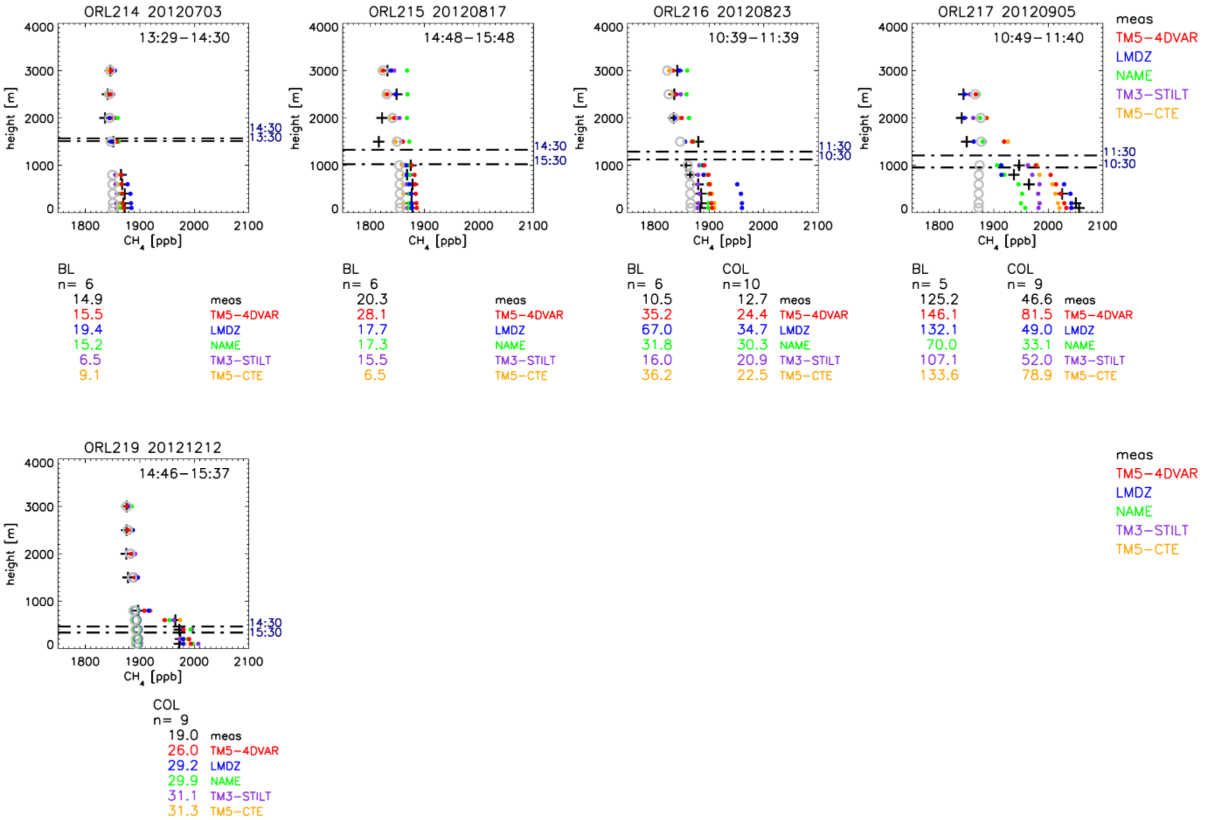

Figure 7S: continued

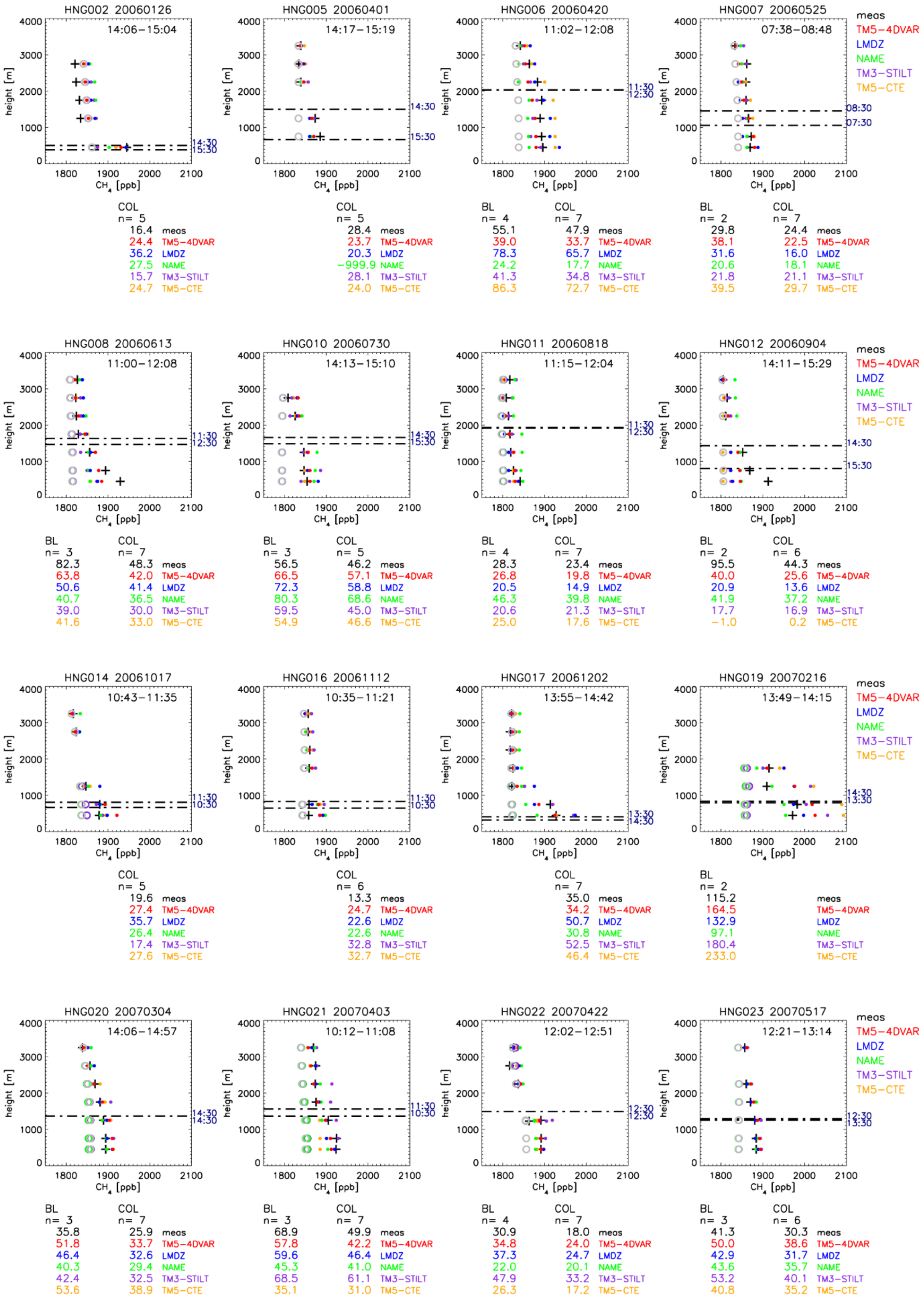

Figure 8S: Individual aircraft profiles from Hegyhátsál (HNG), Hungary. Black crosses: measurements; filled coloured symbols: corresponding model simulations; open circles: simulated background mole fractions, based on the method of *Rödenbeck et al.* [2009], calculated for the TM5 domain (grey), and for the NAME (green) and TM3-STILT (violet) domains (the latter are, however, only partially visible, since they largely overlap with the background for the TM5 domain). Below each panel the calculated enhancements integrated over the entire boundary layer ($\Delta c_{MOD, BL}$ and $\Delta c_{OBS, BL}$) and integrated over the entire profile ($\Delta c_{MOD, COL}$ and $\Delta c_{OBS, COL}$) are given. n denote the number of samples used to evaluate the integrated enhancements. The dash-dotted lines indicate the top of the boundary layer diagnosed by TM5 at the given times.

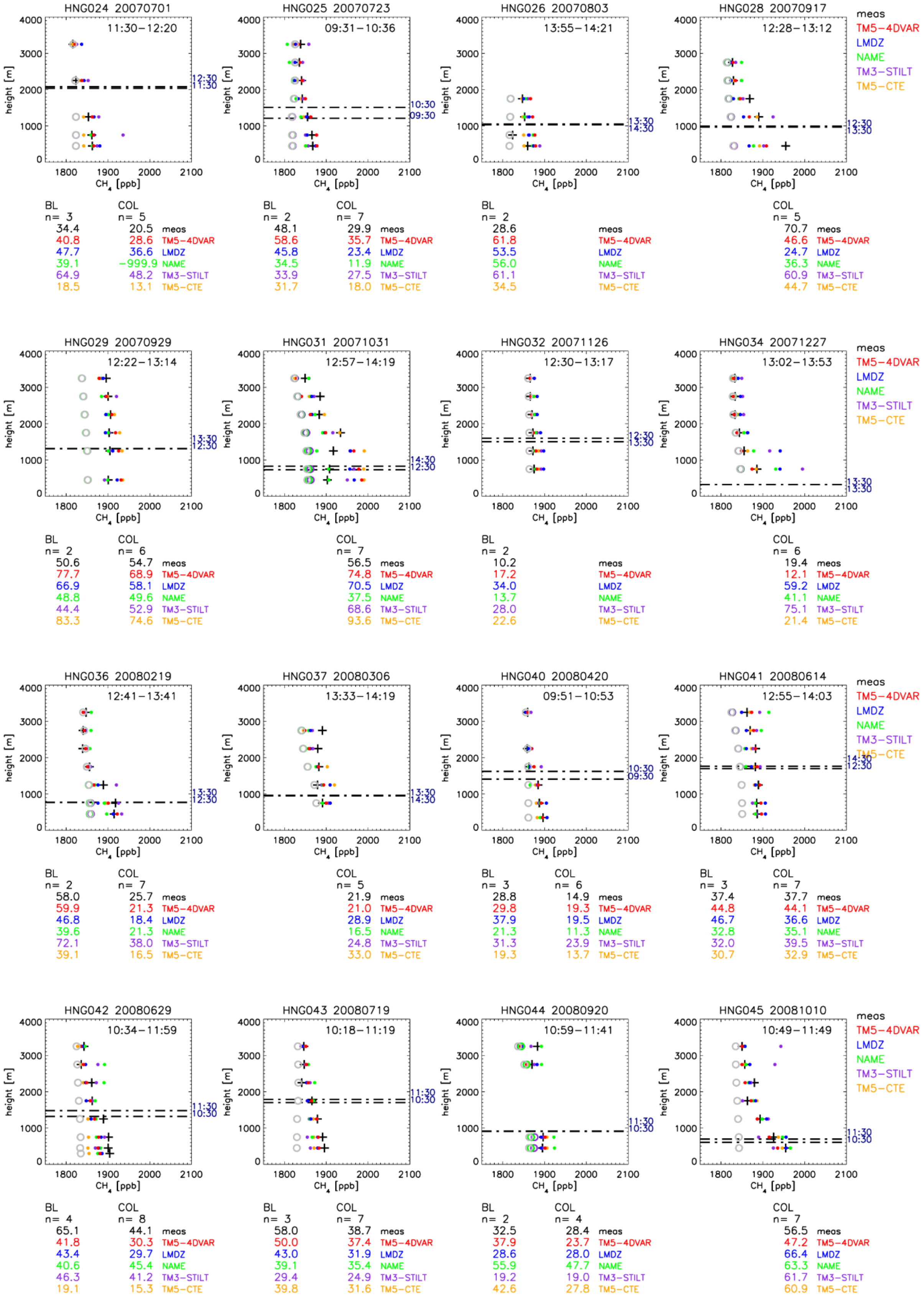

Figure 8S: continued

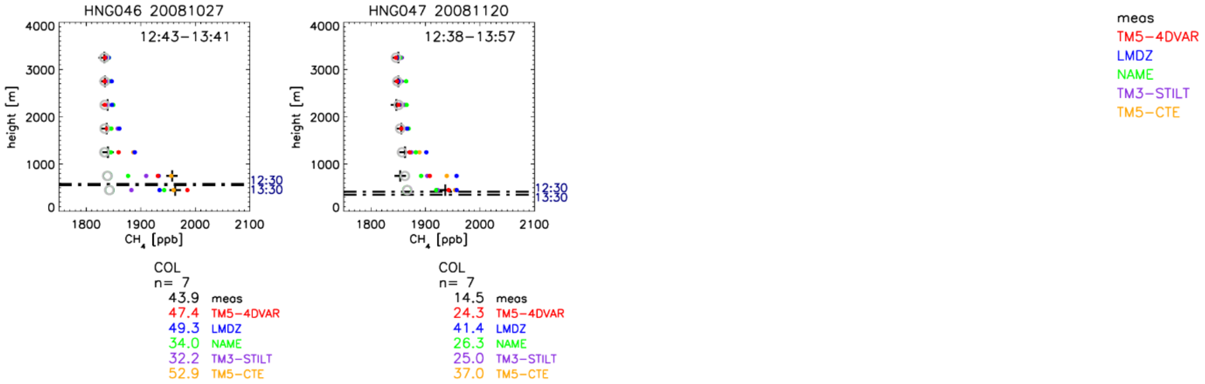

Figure 8S: continued

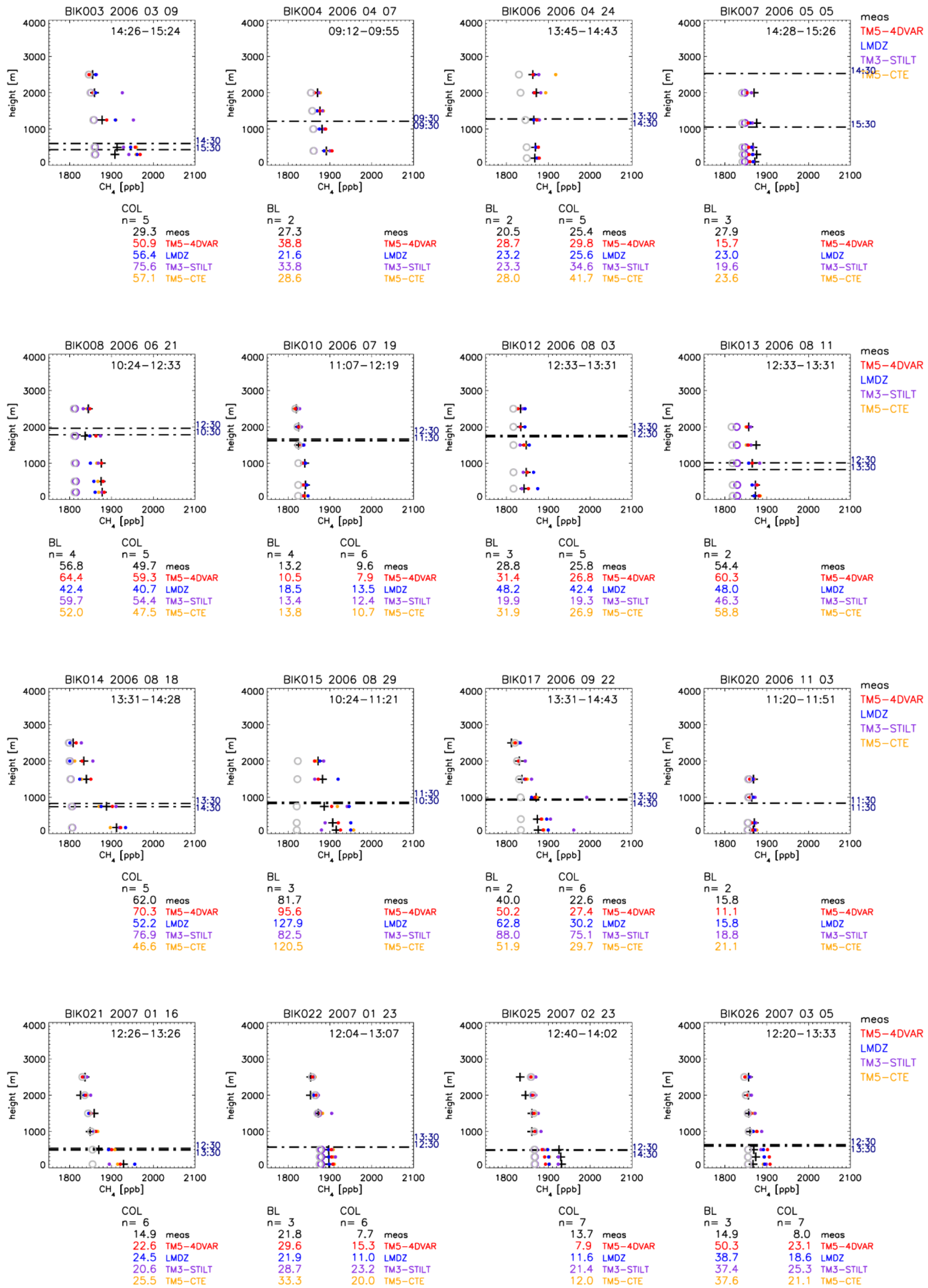

Figure 9S: Individual aircraft profiles from Bialystok (BIK), Poland. Black crosses: measurements; filled coloured symbols: corresponding model simulations; open circles: simulated background mole fractions, based on the method of *Rödenbeck et al.* [2009], calculated for the TM5 domain (grey), and for the NAME (green) and TM3-STILT (violet) domains (the latter are, however, only partially visible, since they largely overlap with the background for the TM5 domain). Below each panel the calculated enhancements integrated over the entire boundary layer ($\Delta c_{MOD,\,BL}$ and $\Delta c_{OBS,\,BL}$) and integrated over the entire profile ($\Delta c_{MOD,\,COL}$ and $\Delta c_{OBS,\,COL}$) are given. n denote the number of samples used to evaluate the integrated enhancements. The dash-dotted lines indicate the top of the boundary layer diagnosed by TM5 at the given times.

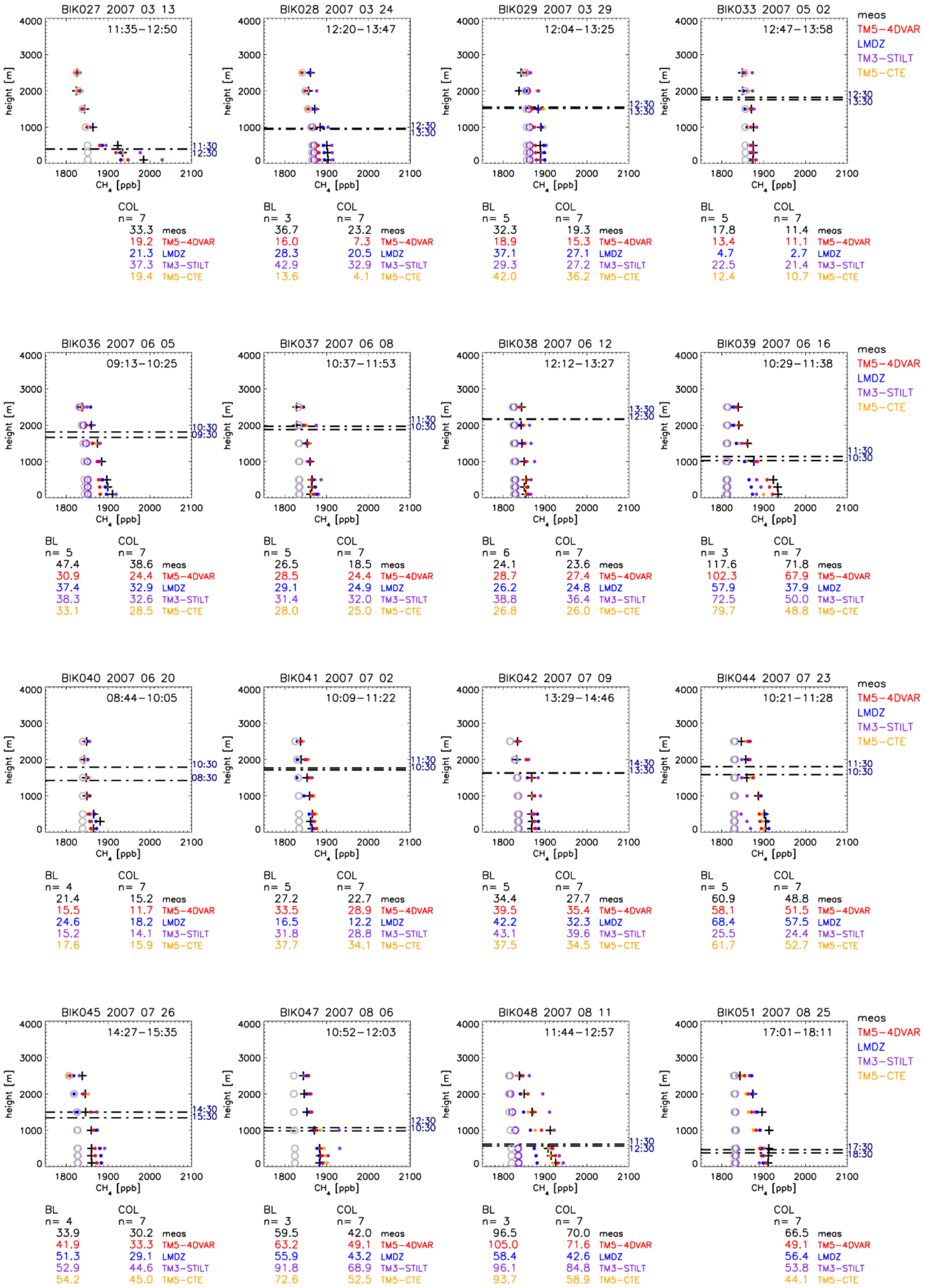

Figure 9S: continued

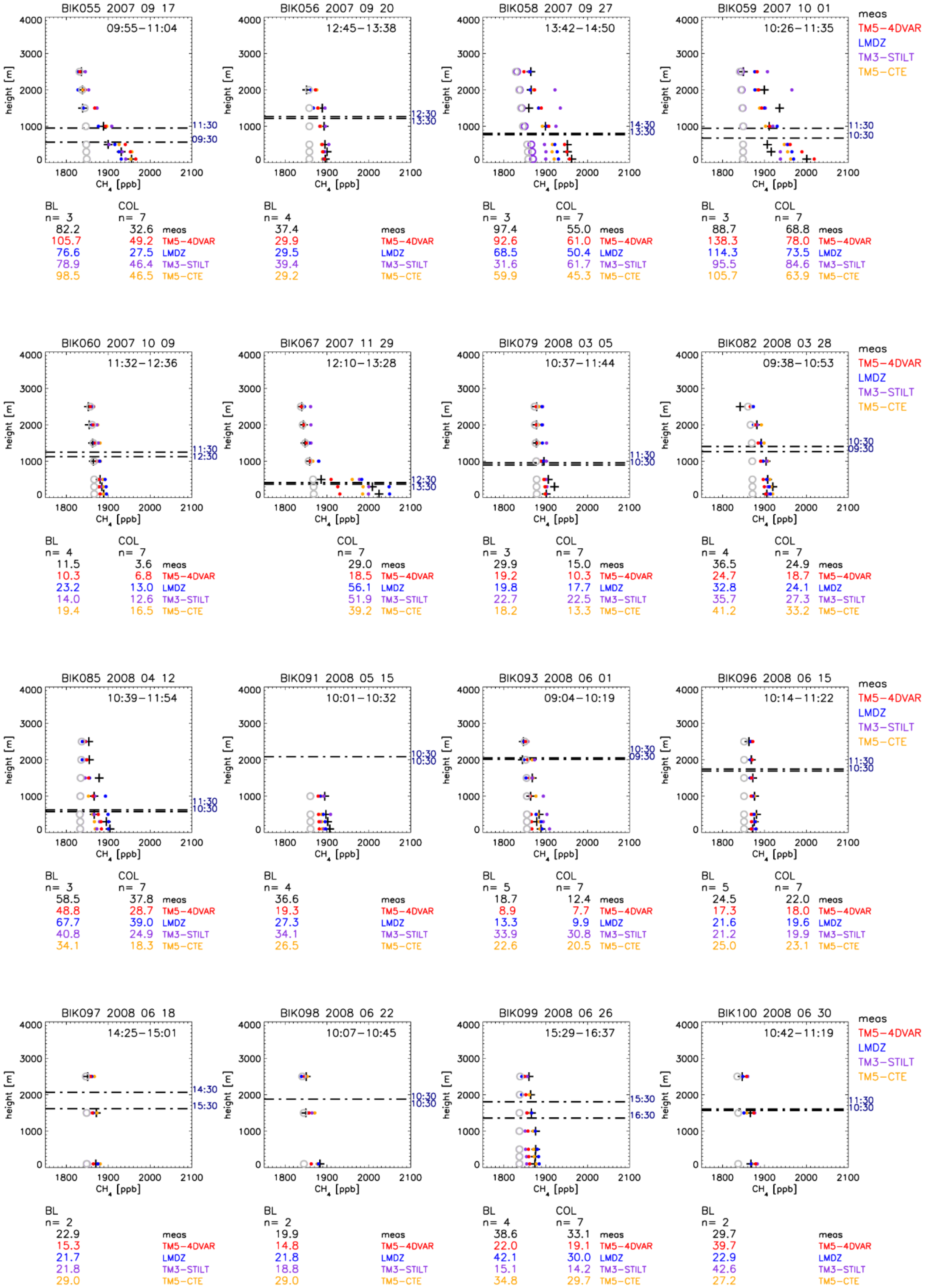

Figure 9S: continued

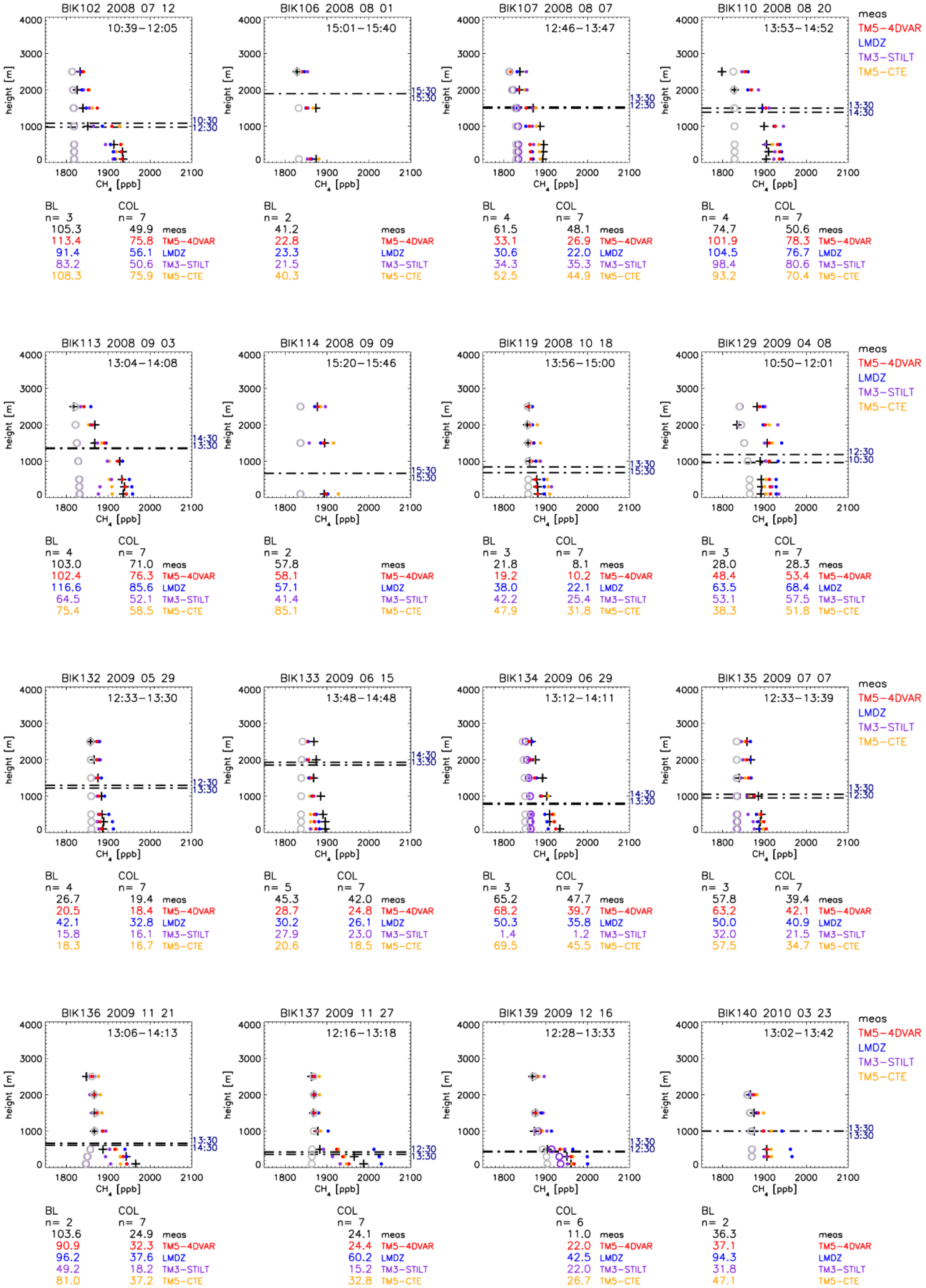

Figure 9S: continued

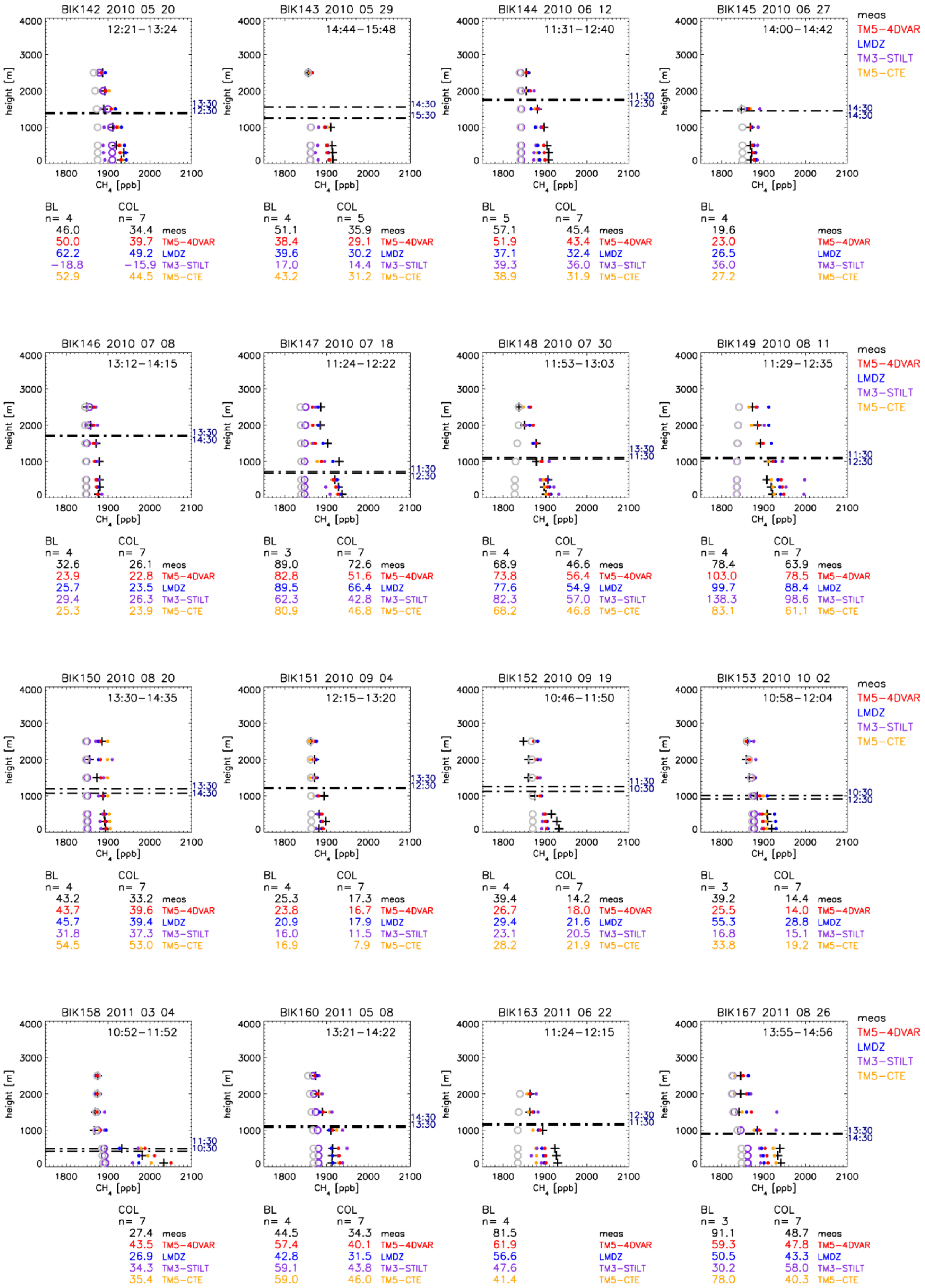

Figure 9S: continued

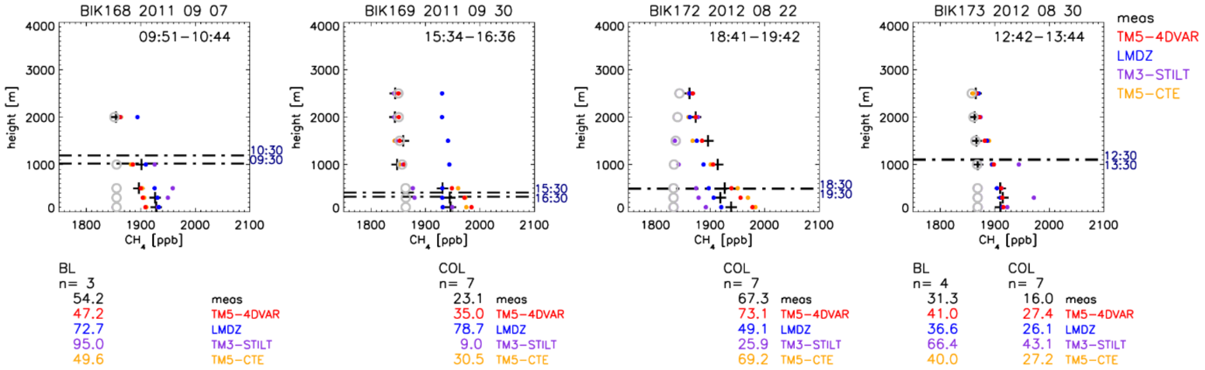

Figure 9S: continued

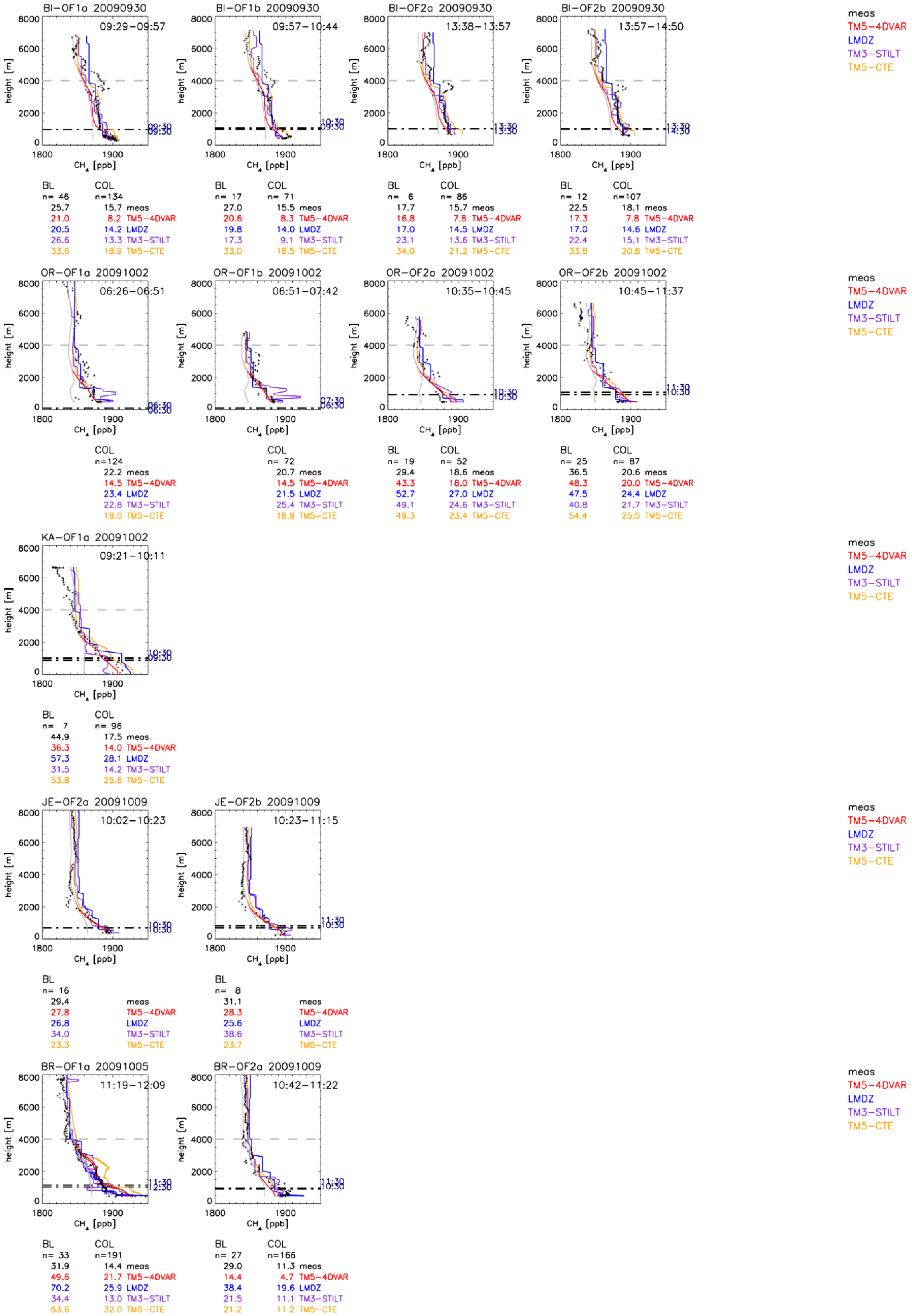

Figure 10S: Individual aircraft profiles from IMECC. Black dots: measurements; coloured lines: corresponding model simulations; grey line: simulated background mole fractions, based on the method of *Rödenbeck et al.* [2009]. Below each panel the calculated enhancements integrated over the entire boundary layer ($\Delta c_{MOD,\,BL}$ and $\Delta c_{OBS,\,BL}$) and integrated over the lower troposphere ($\Delta c_{MOD,\,COL}$ and $\Delta c_{OBS,\,COL}$) are given. n denote the number of samples used to evaluate the integrated enhancements. The dash-dotted lines indicate the top of the boundary layer diagnosed by TM5 at the given times. The grey dashed line indicates the upper boundary (4 km) for the integration over the lower troposphere.

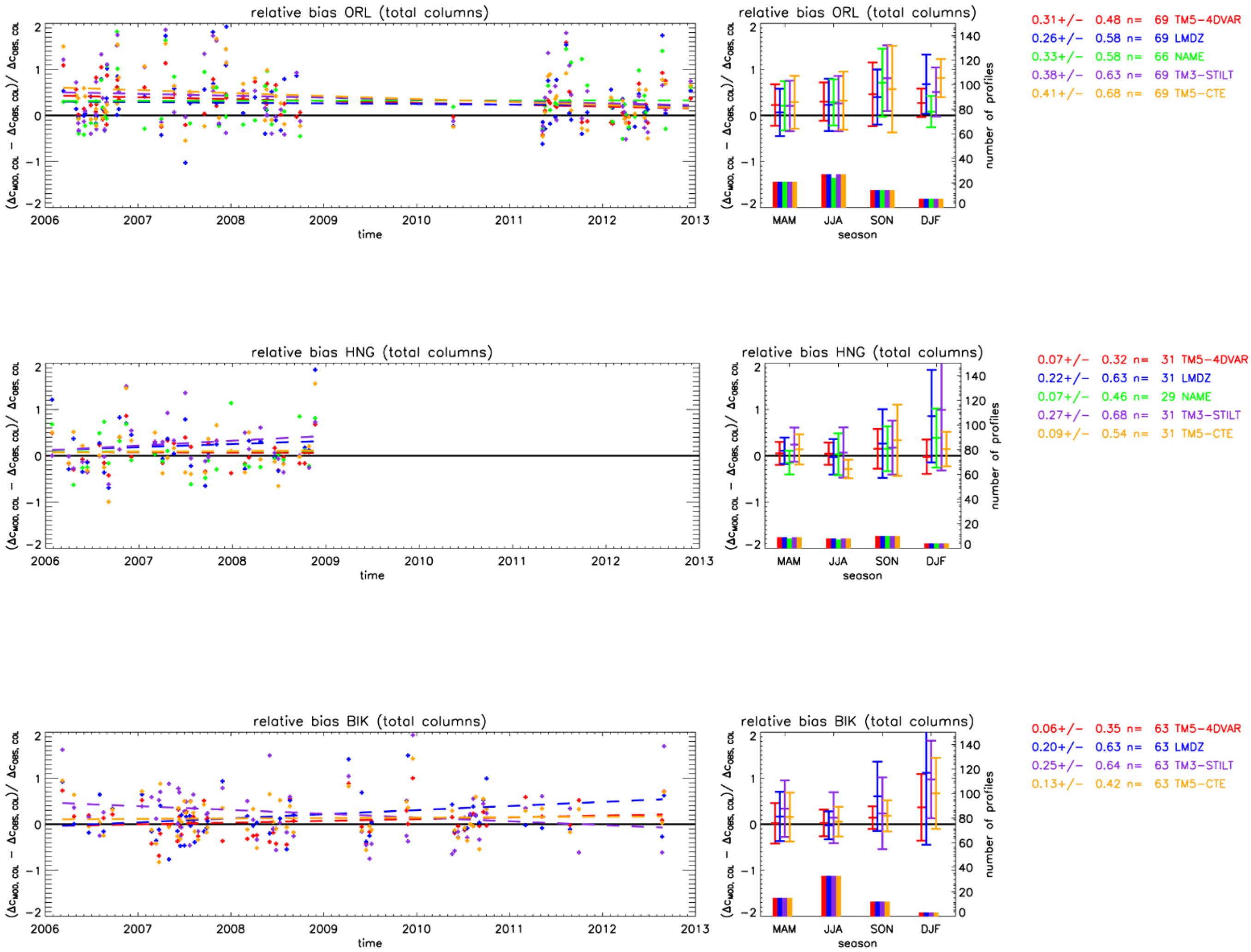

Figure 11S: 'relative' bias within the lower troposphere evaluated from simulated and observed mole fraction enhancements compared to the background (($\Delta c_{MOD,\,COL}$ - $\Delta c_{OBS,\,COL}$) / $\Delta c_{OBS,\,COL}$); see section 4.2). Left: time series; right: seasonal averages with numbers of available profiles given as bargraphs (see right axis). The numbers on the right side are the average relative bias, 1σ standard deviation, and total number of profiles over the entire period.

References

Berchet, A., I. Pison, F. Chevallier, P. Bousquet, J.-L. Bonne, and J.-D. Paris, Objectified quantification of uncertainties in Bayesian atmospheric inversions, Geosci. Model Dev., *Geosci. Model Dev.*, *8*, 1525-1546, doi: 10.5194/gmd-8-1525-2015, 2015a.

Berchet, A., et al., Natural and anthropogenic methane fluxes in Eurasia: a mesoscale quantification by generalized atmospheric inversion, *Biogeosciences*, *12*, 5393–5414, doi: 10.5194/bg-12-5393-2015, 2015b.

Bergamaschi, P., et al., Inverse modeling of European CH_4 emissions 2001-2006, *J. Geophys. Res.*, *115*(D22309), doi:10.1029/2010JD014180, 2010.

Bergamaschi, P., et al., Top-down estimates of European CH_4 and N_2O emissions based on four different inverse models, *Atmos. Chem. Phys.*, *15*, 715-736, doi: 10.5194/acp-15-715-2015, 2015.

Bousquet, P., et al., Source attribution of the changes in atmospheric methane for 2006–2008, *Atmos. Chem. Phys.*, *11*, 3689–3700, doi: 10.5194/acp-11-3689-2011, 2011.

Brühl, C., and P. J. Crutzen, The MPIC 2D model, in *NASA Ref. Publ. 1292, vol 1*, pp. 103-104, 1993.

Chevallier, F., M. Fisher, P. Peylin, S. Serrar, P. Bousquet, F.-M. Bréon, A. Chédin, and P. Ciais, Inferring CO_2 sources and sinks from satellite observations: Method and application to TOVS data, *J. Geophys. Res.*, *110*(D24309), doi:10.1029/2005JD006390, 2005.

Dee, D. P., On-line estimation of error covariance parameters for atmospheric data assimilation, *Mon. Weather Rev.*, *123*, 1128–1145, 1995.

Dee, D. P., et al., The ERA-Interim reanalysis: configuration and performance of the data assimilation system, *Q. J. R. Meteorol. Soc.*, *137*, 553–597, doi: 10.1002/qj.828, 2011.

Eisma, R., A. T. Vermeulen, and K. van der Borg, $^{14}CH_4$ emissions from nuclear power plants in Northwestern Europe, *Radiocarbon 37* (2), 475-483, 1995.

Evensen, G., The Ensemble Kalman Filter: theoretical formulation and practical implementation, *Ocean Dynam.*, *53*(4), 343–367, doi: 10.1007/s10236-003-0036-9, 2003.

Gerbig, C., J. Lin, S. Wofsy, B. Daube, A. Andrews, B. Stephens, P. Bakwin, and C. Grainger, Toward constraining regional-scale fluxes of CO_2 with atmospheric observations over a continent: 2. Analysis of COBRA data using a receptor-oriented framework, *J. Geophys. Res.*, *108*, 4757, doi: 10.1029/2003JD003770, 2003.

Gilbert, J. C., and C. Lemaréchal, Some numerical experiments with variable-storage quasi-Newton algorithms. Mathematical Programming, *Mathematical Programming*, *45*, 407-435, 1989.

Heimann, M., and S. Koerner, The Global Atmospheric Tracer Model TM3, Tech. Rep. 5 J. Max-Planck-Institut für Biogeochemie, Germany, Jena, Germany, http://www.bgc-jena.mpg.de/uploads/Publications/TechnicalReports/tech_report5.pdf, 2003.

Holtslag, A. A. M., and C.-H. Moeng, Eddy diffusivity and counter-gradient transport in the convective atmospheric boundary layer, *J. Atmos. Sci.*, *48*, 1690-1698, 1991.

Hourdin, F., and A. Armengaud, The use of finite-volume methods for atmospheric advection of trace species. Part I: Test of various formulations in a general circulation model, Monthly Weather Review, *Monthly Weather Review*, *127*(5), 822-837, 1999.

Hourdin, F., et al., The LMDZ4 general circulation model: climate performance and sensitivity to parameterized physics with emphasis on tropical convection, *Clim. Dyn.*, *27*, 787-813, doi: 10.1007/s00382-006-0158-0, 2006.

Houweling, S., et al., A multi-year methane inversion using SCIAMACHY, accounting for systematic errors using TCCON measurements, *Atmos. Chem. Phys.*, *14*, 3991–4012, doi: 10.5194/acp-14-3991-2014, 2014.

Ito, A., and M. Inatomi, Use of a process-based model for assessing the methane budgets of global terrestrial ecosystems and evaluation of uncertainty, *Biogeosciences*, *9*(2), 759-773, doi: 10.5194/bg-9-759-2012, 2012.

Koffi, E. N., et al., Evaluation of the boundary layer dynamics of the TM5 model over Europe, *Geosci Model Dev*, *9*, 3137-3160, doi: 10.5194/gmd-9-3137-2016, 2016.

Krol, M., S. Houweling, B. Bregman, M. van den Broek, A. Segers, P. van Velthoven, W. Peters, F. Dentener, and P. Bergamaschi, The two-way nested global chemistry-transport zoom model TM5: algorithm and applications, *Atmos. Chem. Phys.*, *5*, 417-432, doi: 10.5194/acp-5-417-2005, 2005.

Krol, M. C., J. F. Meirink, P. Bergamaschi, J. E. Mak, D. Lowe, P. Jöckel, S. Houweling, and T. Röckmann, What can ^{14}CO measurements tell us about OH?, *Atmos. Chem. Phys.*, *8*, 5033–5044, doi: 10.5194/acp-8-5033-2008, 2008.

Lambert, G., and S. Schmidt, Reevaluation of the oceanic flux of methane: Uncertainties and long term variations, *Chemosphere: Global Change Science*, *26*(no. 1-4), 579-589, 1993.

Lin, J. C., C. Gerbig, S. C. Wofsy, A. E. Andrews, B. C. Daube, K. J. Davis, and C. A. Grainger, A near-field tool for simulating the upstream influence of atmospheric observations: The Stochastic Time-Inverted Lagrangian Transport (STILT) model, *J. Geophys. Res.*, *108*, 4493, doi: 10.1029/2002JD003161, 2003.

Louis, J. F., A parametric model of vertical eddy fluxes in the atmosphere, *Boundary Layer Meteorology*, *17*, 187-202, 1979.

Manning, A. J., S. O'Doherty, A. R. Jones, P. G. Simmonds, and R. G. Derwent, Estimating UK methane and nitrous oxide emissions from 1990 to 2007 using an inversion modeling approach, *J. Geophys. Res.*, *116*(D02305), doi:10.1029/2010JD014763, 2011.

Meirink, J. F., P. Bergamaschi, and M. Krol, Four-dimensional variational data assimilation for inverse modelling of atmospheric methane emissions: Method and comparison with synthesis inversion, *Atmos. Chem. Phys.* , *8*, 6341–6353, doi: 10.5194/acp-8-6341-2008, 2008.

Melton, J. R., et al., Present state of global wetland extent and wetland methane modelling: conclusions from a model inter-comparison project (WETCHIMP), *Biogeosciences*, *10*(2), 753-788, doi: 10.5194/bg-10-753-2013, 2013.

Menut, L., et al., CHIMERE 2013: a model for regional atmospheric composition modelling, *Geosci. Model Dev.*, *6*, 981–1028, doi: 10.5194/gmd-6-981-2013, 2013.

Patra, P. K., et al., TransCom model simulations of CH_4 and related species: linking transport, surface flux and chemical loss with CH_4 variability in the troposphere and lower stratosphere, *Atmos. Chem. Phys.*, *11*, 12813–12837, doi: 10.5194/acp-11-12813-2011, 2011.

Pison, I., P. Bousquet, F. Chevallier, S. Szopa, and D. Hauglustaine, Multi-species inversion of CH_4, CO and H_2 emissions from surface measurements, *Atmos. Chem. Phys.*, *9*, 5281–5297, doi: 10.5194/acp-9-5281-2009, 2009.

Press, W. H., S. A. Teukolsky, W. T. Vetterling, and B. P. Flannery, *Numerical recipes in C: The art of scientific computing, Second Edition*, Cambridge University Press, 1992.

Randerson, J. T., G. R. van der Werf, L. Giglio, G. J. Collatz, and P. S. Kasibhatla, Global Fire Emissions Database, Version 3 (GFEDv3.1), Oak Ridge National Laboratory Distributed Active Archive Center, Oak Ridge, Tennessee, USA, http://daac.ornl.gov/, 2013.

Ravela, S., and D. McLaughlin, Fast ensemble smoothing, *Ocean Dynamics*, *57*(2), 123–134, doi: 10.1007/s10236-006-0098-6,, 2007.

Rödenbeck, C., Estimating CO_2 sources and sinks from atmospheric mixing ratio measurements using a global inversion of atmospheric transport, Tech. Rep. 6, Max-Planck-Institut für Biogeochemie, Jena, http://www.bgc-jena.mpg.de/mpg/website Biogeochemie/Publikationen/Technical Reports/tech report6.pdf., http://www.bgc-jena.mpg.de/uploads/Publications/TechnicalReports/tech_report6.pdf, 2005.

Rödenbeck, C., C. Gerbig, K. Trusilova, and M. Heimann, A two-step scheme for high-resolution regional atmospheric trace gas inversions based on independent models, *Atmos. Chem. Phys.*, *9*, 5331–5342, doi: 10.5194/acp-9-5331-2009, 2009.

Spahni, R., F. Joos, B. D. Stocker, M. Steinacher, and Z. C. Yu, Transient simulations of the carbon and nitrogen dynamics in northern peatlands: from the Last Glacial Maximum to the 21st century, *Clim. Past*, *9*(3), 1287–1308, doi: 10.5194/cp-9-1287-2013, 2013.

Spivakovsky, C. M., et al., Three-dimensional climatological distribution of tropospheric OH: Update and evaluation, *J. Geophys. Res.*, *105*(D7), 8931– 8980, 2000.

Stohl, A., and P. Seibert, Accuracy of trajectories as determined from the conservation of meteorological tracers, *Q. J. R. Meteorol. Soc.*, *124*, 1465-1484, 1998.

Tiedtke, M., A comprehensive mass flux scheme for cumulus parameterization in large-scale models, *Monthly Weather Review*, *117*, 1779-1800, 1987.

Trusilova, K., C. Rödenbeck, C. Gerbig, and M. Heimann, Technical Note: a new coupled system for global-to-regional downscaling of CO_2 concentration estimation, *Atmos. Chem. Phys.*, *10*, 3205–3213, doi: 10.5194/acp-10-3205-2010, 2010.

Tsuruta, A., et al., Development of CarbonTracker Europe-CH_4; Part 2: global methane emission estimates and their evaluation for 2000-2012, *Geoscientific Model Development Discussions*, 1-52, doi: 10.5194/gmd-2016-182, 2016.

van der Werf, G. R., J. T. Randerson, L. Giglio, G. J. Collatz, M. Mu, P. S. Kasibhatla, D. C. Morton, R. S. DeFries, Y. Jin, and T. T. van Leeuwen, Global fire emissions and the contribution of deforestation, savanna, forest, agricultural, and peat fires (1997–2009), *Atmos. Chem. Phys.*, *10*, 11707–11735, doi: 10.5194/acp-10-11707-2010, 2010.

Vermeulen, A., R. Eisma, A. Hensen, and J. Slanina, Transport model calculations of NW European methane emissions, *Env. Sci. & Policy*, *2*, 315-324, 1999.

Vermeulen, A. T., G. Pieterse, A. Hensen, W. C. M. van den Bulk, and J. W. Erisman, COMET: a Lagrangian transport model for greenhouse gas emission estimation – forward model technique and performance for methane, *Atmos. Chem. Phys. Discuss.*, *6*, 8727-8779, doi: 10.5194/acpd-6-8727-2006, 2006.

Wania, R., et al., Present state of global wetland extent and wetland methane modelling: methodology of a model inter-comparison project (WETCHIMP), *Geosci Model Dev*, *6*(3), 617-641, doi: 10.5194/gmd-6-617-2013, 2013.